



# The Route to Unveil the Cosmic Genealogy of Supermassive Black Hole Binaries Using Nano-Hertz Gravitational Waves and Galaxy Surveys

Mohit Raj Sah<sup>1</sup>, Suvodip Mukherjee<sup>1</sup>

<sup>1</sup>*Department of Astronomy and Astrophysics, Tata Institute of Fundamental Research, Mumbai 400005, India*

9 April 2025

## ABSTRACT

The nano-hertz (nHz) stochastic gravitational wave background (SGWB), produced by unresolved supermassive black hole binaries (SMBHBs), offers a unique probe of their cosmic evolution. Using our recently proposed technique, we investigate the prospect of discovering the SMBHB population and its evolution by combining the SGWB signal and its anisotropies with galaxy observation by exploring their cross-correlation. Using a Fisher analysis, we demonstrate that the SGWB power spectrum alone can provide only a weak measurement of the cosmic genealogy of SMBHBs, while the inclusion of the angular power spectrum of SGWB and its cross-correlation with the galaxy distribution can significantly improve our measurement and open a discovery space. With a PTA of 2000 pulsars, achievable in the SKA era, we find that the redshift evolution of the supermassive black hole (SMBH) mass and galaxy stellar mass can be measured with an SNR up to 4 in the redshift range up to three. The frequency distribution can be constrained with an SNR of approximately up to 80 in the same redshift range at a frequency range accessible from nHz. These SNRs improve further with the increase in the number of pulsars to 5000 expected from SKA. This demonstrates the prospect of answering the decades-long unsolved problem of SMBH growth and evolution over cosmic time and shedding new insights on the standard model of cosmology using synergy between nHz GW and galaxy surveys.

**Key words:** gravitational waves, black hole mergers, galaxy, cosmology: miscellaneous

## 1 INTRODUCTION

Pulsar Timing Arrays (PTAs) have opened a new observational window for studying nano-hertz (nHz) gravitational waves (GWs), whose primary source is believed to be the inspiraling supermassive black hole binaries (SMBHBs). By accurately measuring the arrival times of radio pulses from millisecond pulsars, PTA collaborations worldwide, which include the European PTA (EPTA; [Desvignes et al. \(2016\)](#)), the North American Observatory for Gravitational Waves (NANOGrav; [McLaughlin \(2013\)](#)), the Parkes PTA (PPTA; [Manchester et al. \(2013\)](#)), the Indian PTA (InPTA; [Joshi et al. \(2018\)](#)), and the Chinese PTA (CPTA; [Xu et al. \(2023\)](#)), are actively searching for the nanohertz (nHz) stochastic gravitational wave background (SGWB). Their efforts have led to compelling evidence of nHz SGWB

([Agazie et al. 2023b](#); [Antoniadis et al. 2023](#); [Zic et al. 2023](#); [Xu et al. 2023](#)).

The formation and evolution of SMBHBs remain a long-standing question in astrophysics ([Volonteri 2007, 2010](#); [Latif & Ferrara 2016](#); [Volonteri et al. 2021](#)). The study of nHz GWs offers a unique opportunity to investigate their population and cosmic evolution ([Feng et al. 2020](#); [Padmanabhan & Loeb 2023](#); [Agazie et al. 2023a](#); [Sah et al. 2024](#); [Sah & Mukherjee 2024](#); [Sato-Polito et al. 2025](#)). SMBHBs are believed to be a byproduct of galaxy mergers, where the gravitational interactions between merging galaxies bring their central SMBHBs closer together, eventually forming a binary system. As these binaries lose energy through mechanisms such as dynamical friction, stellar scattering, and viscous drag, they eventually enter the GW-emitting regime, producing signals detectable in the PTA band ([Sampson et al. 2015](#); [Kelley et al. 2017](#); [Chen et al. 2017](#); [Izquierdo-Villalba et al. 2022](#)). The study of these GWs provides a direct probe of the SMBHB population, shedding light on their mass distribution, merger rates, and correlations with the properties

† mohit.sah@tifr.res.in

‡ suvodip@tifr.res.in

of their host galaxies. Moreover, such investigations enable a deeper understanding of the cosmic evolution of SMBHBs across redshift (Sah et al. 2024; Sah & Mukherjee 2024).

The SGWB is characterized by its frequency-dependent energy density spectrum (represented by  $\Omega_{\text{GW}}(f)$ ). This spectrum can provide valuable information about the sources of the SGWB. However, this spectrum alone is insufficient to constrain the wide range of properties associated with the SMBHB population. To obtain deeper insights, the SGWB must be further analyzed through its anisotropies. The anisotropy in the SGWB signal is typically quantified using the auto-angular power spectrum,  $C_\ell^{\text{GWGW}}$ , which characterizes the spatial distribution of the GW background across the sky (Mingarelli et al. 2013; Agazie et al. 2023b; Sato-Polito & Kamionkowski 2024; Raidal et al. 2024). However, the anisotropy is likely to be non-Gaussian, and  $C_\ell^{\text{GWGW}}$  is expected to be dominated by shot noise (Sah et al. 2024). Sah & Mukherjee (2025) proposed a novel technique for detecting the anisotropic SGWB, in which the anisotropic SGWB is directly stacked in regions of galaxy overdensity using a galaxy catalog as a tracer. Recently, Sah & Mukherjee (2024) demonstrated the use of the cross-angular power spectrum ( $C_\ell^{\text{gGW}}$ ) between the nHz SGWB and galaxy catalogs. It was shown that the  $C_\ell^{\text{gGW}}$  carries the imprint of the cosmic evolution of the SMBH population. By leveraging galaxy survey data, such as those from the Rubin LSST Observatory (Ivezić et al. 2019), we can probe the evolution of the SMBHB population and their host galaxies over cosmic time (Sah & Mukherjee 2024).

In this work, we aim to assess the feasibility of using the SGWB power spectrum combined with its anisotropy to constrain the properties and evolution of the SMBHB population. By utilizing different configurations of future PTAs in combination with next-generation galaxy surveys, we evaluate the potential to extract robust constraints on the SMBHB population. We found that the SGWB power spectrum alone is inadequate for constraining SMBHB properties due to parameter degeneracies. However, incorporating the information from anisotropy in the signal significantly improves parameter estimation by breaking these degeneracies, enabling a more detailed characterization of the SMBHB population. Notably, the impact of anisotropy information depends on the SMBHB population model and the redshift evolution of the SMBHBs.

The paper is organized as follows: in Sec. 2, we discuss the SMBHB population model as well as the SGWB generated by the population; in Sec. 3, we discuss the angular power spectrum of the SGWB signal and its cross-correlation with the galaxy distribution; in Sec. 4, we explore how population parameters influence different components of the cross-correlation curve; in Sec. 5, we review the cross-correlation of PTA timing residuals and the various noise components affecting these measurements; in Sec. 6, we present the result of the Fisher analysis. Finally, in Sec. 7, we discuss the conclusions and future prospects.

## 2 SGWB FROM SMBHB POPULATION AND GALAXY DISTRIBUTION

The SGWB density from a population of SMBHB in unit solid angle can be written as (Phinney 2001; Sesana et al.

2008; Christensen 2018)

$$\Omega_{\text{GW}}(f, \hat{n}) = \frac{1}{4\pi\rho_c c^2} \iint dV dM_{\text{BH}} dq \left[ f_r \kappa(M_{\text{BH}}, q, a|z) n_v(z, \hat{n}) \right] \times \left[ \frac{1}{4\pi d_\ell^2(z)c} \frac{dE_{\text{gw}}(a, M_{\text{BH}}, q, z)}{dt_r} \right], \quad (1)$$

where  $M_{\text{BH}}$  is the primary mass and  $q$  is the mass ratio of the binary.  $f_r$  ( $\equiv f/(1+z)$ ) is the source frame frequency,  $d_\ell$  is the luminosity distance,  $n_v(z, \hat{n})$  represents the number of SMBHBs per unit comoving volume in the direction  $\hat{n}$ , and  $\frac{dE_{\text{gw}}(f_r, M_{\text{BH}}, q, z)}{dt_r}$  is the GW luminosity emitted by a binary of mass  $M_{\text{BH}}$ , and mass ratio  $q$ . Finally,  $\kappa(M_{\text{BH}}, q, f_r | z)$  denotes the mean number of SMBHBs per galaxy, at redshift  $z$ , with primary mass  $M_{\text{BH}}$ , mass ratio  $q$ , and emitting at rest-frame frequency  $f_r$ . This distribution is modeled as

$$\begin{aligned} \kappa(M_{\text{BH}}, q, f_r | z) &= \mathcal{N} \int dM_* P(M_* | z) P(M_{\text{BH}}, q, f_r | M_*, z) \\ &= \mathcal{N} \int dM_* P(M_* | z) P(M_{\text{BH}} | M_*, z) \\ &\quad P(q | M_*, z) P(f_r | M_*, z), \end{aligned} \quad (2)$$

where  $\mathcal{N}$  is the normalization constant that quantifies the occupation fraction of SMBHBs in galaxies,  $P(M_* | z)$  is the stellar mass function of the galaxy, and  $P(M_{\text{BH}} | M_*, z)$  is modeled as a Gaussian distribution of the logarithm of the SMBH mass, conditioned on the stellar mass of the host galaxy

$$P(M_{\text{BH}} | M_*, z) = \frac{1}{\sqrt{2\pi}\sigma} \exp\left(-\frac{(\text{Log}_{10}(M_{\text{BH}}) - \text{Log}_{10}(\tilde{M}_{\text{BH}}))^2}{2\sigma^2}\right), \quad (3)$$

where

$$\text{Log}_{10}(\tilde{M}_{\text{BH}}) = \eta + \rho \text{Log}_{10}(M_*/10^{11} M_\odot) + \nu z, \quad (4)$$

with  $\eta$ ,  $\rho$ , and  $\nu$  being free parameters governing the scaling relation. The probability distributions for the mass ratio,  $P(q | M_*, z)$  is modeled as

$$P(q | M_*, z) \propto \begin{cases} 1/q, & 0.01 < q < 1, \\ 0, & \text{else.} \end{cases} \quad (5)$$

For the entire analysis in this paper, we adopt the simplifying assumption of circular orbits. Consequently, each binary system emits GW monochromatically. Under this assumption, we model the source-frame frequency distribution,  $P(f_r | M_*, z)$ , as

$$P(f_r | M_*, z) \propto f_r^{\alpha + z\lambda}, \quad (6)$$

where the parameters  $\alpha$ , and  $\lambda$  govern the frequency distribution and its redshift evolution. Astrophysical processes such as binary stalling or environmental coupling can modify the frequency distribution  $P(f_r | M_*, z)$  (Sampson et al. 2015; Kelley et al. 2017; Chen et al. 2017). The occupation fraction of GW sources within each frequency bin, expressed in terms of the spectral parameters  $\alpha$  and  $\lambda$ , effectively encapsulates these effects and their evolution with redshift.

In Fig. 1, we show the SGWB spectral density,  $\Omega_{\text{GW}}(f)$ , for different values of  $\eta$ ,  $\nu$ ,  $\alpha$ , and  $\lambda$ . We assume the redshift distribution of galaxies ( $\frac{dn}{dz}$ ) is similar to LSST-like surveys (Carretero et al. 2017; Tallada et al. 2020). The normalization constant,  $\mathcal{N}$ , is chosen such that the spectrum attains

a fixed value at a reference frequency,  $f_{\text{ref}}$ . In this case, we set this value to the median value of the power law curve at  $f = 6 \times 10^{-9}$  Hz fitted to the 15-year data release of NANOGrav (Agazie et al. 2023b).

The curves in Fig. 1 highlight the sensitivity of  $\Omega_{\text{GW}}(f)$  to variations in the parameters. Notably, the spectrum is highly insensitive to changes in  $\eta$ ,  $\rho$ , and  $\nu$ . This is because these parameters control the amplitude of the signal, which is fixed by the amplitude at a reference frequency ( $f_{\text{ref}} = 6 \times 10^{-9}$  Hz). This behavior introduces a degeneracy between  $\eta$ ,  $\rho$ , and  $\nu$ , making it challenging to distinguish their individual contributions using  $\Omega_{\text{GW}}(f)$  alone. In contrast, both  $\alpha$  and  $\lambda$  influence the shape of the spectrum. The parameter  $\eta$  sets the minimum mass of the BHs.  $\nu$  controls the redshift evolution of the mass of the BHs. A negative  $\nu$  implies that at higher redshifts, galaxies of similar mass tend to host relatively lower-mass BHs, whereas a positive  $\nu$  suggests that at higher redshifts, galaxies of similar mass tend to host comparatively more massive BHs. The parameters  $\alpha$  and  $\lambda$  define the frequency distribution of BHs, with  $\lambda$  governing its redshift evolution. A positive  $\lambda$  implies that at higher redshifts, there is a relative increase in the number of BHs emitting at higher frequencies, whereas a negative  $\lambda$  indicates that at higher redshifts, there are relatively more binaries emitting at lower frequencies.

### 3 ANISOTROPIC SGWB SIGNAL

This section describes the formalism of the anisotropic SGWB signal which includes the auto-angular power spectrum of the SGWB as well as its cross-correlation with the galaxy distribution. The cross-correlation is obtained between the spatial overdensity in galaxy number count ( $\delta_g(\hat{n})$ ) and the SGWB ( $\delta_{\text{GW}}(f, \hat{n})$ ). The spatial over density in the  $\Omega_{\text{GW}}(f, \hat{n})$  can be defined as (Sah et al. 2024; Sah & Mukherjee 2024)

$$\delta_{\text{GW}}(f, \hat{n}) \equiv \frac{\Omega_{\text{GW}}(f, \hat{n}) - \bar{\Omega}_{\text{GW}}(f)}{\bar{\Omega}_{\text{GW}}(f)}, \quad (7)$$

which can be rewritten as

$$\delta_{\text{GW}}(f, \hat{n}) = \int dz \delta_m(z, \hat{n}) b_g(z) \phi_{\text{GW}}(f, z), \quad (8)$$

$\delta_m(z, \hat{n})$  is the matter density fluctuation,  $b_g(z)$  is the galaxy bias, which modulates how galaxies trace the underlying matter density, and  $\phi_{\text{GW}}(z)$  is the GW window function given by

$$\phi_{\text{GW}}(f, z) = \frac{\int \frac{d\theta}{d\ell} \left[ f_r \kappa(\theta, f_r | z) \frac{dn}{dz} \right] \left[ \frac{dE_{\text{GW}}(f_r, \theta, \hat{n})}{dt_r} \right]}{\int dz \int \frac{d\theta}{d\ell} \left[ f_r \kappa(\theta, f_r | z) \frac{dn}{dz} \right] \left[ \frac{dE_{\text{GW}}(f_r, \theta, \hat{n})}{dt_r} \right]}, \quad (9)$$

where  $\theta$  represents the set of source properties,  $\frac{dn}{dz}$  represents the redshift distribution of the galaxy. The fluctuations in the SGWB ( $\delta_{\text{GW}}(\hat{n})$ ) and galaxy density ( $\delta_g(\hat{n})$ ) can be expressed in the spherical harmonic basis as

$$\delta_{g, \text{GW}}(\hat{n}) = \sum_{\ell} \sum_{m=-\ell}^{\ell} c_{\ell m}^{\text{g, GW}} Y_{\ell m}(\hat{n}). \quad (10)$$

The angular power spectrum of the SGWB is expected to be dominated by shot noise (Sah et al. 2024). This behavior arises due to the discrete nature of the GW sources,

where the finite number of contributing sources introduces stochastic fluctuations that overshadow any intrinsic clustering signal. The auto-angular power spectrum for the shot noise-dominated signal can be written as

$$C_{\ell}^{\text{GWGW}}(f) \sim \langle \delta_{\text{GW}}^2(f, \hat{n}) \rangle, \quad (11)$$

and the uncertainty in the measurement of the  $C_{\ell}^{\text{GWGW}}(f)$  signal,  $\Sigma_{\text{GWGW}}^2(f, \ell)$ , for a Gaussian signal is given by

$$\Sigma_{\text{GWGW}}^2(f, \ell) = \frac{2}{f_{\text{sky}}(2\ell + 1)} \left[ \left( C_{\ell}^{\text{GWGW}}(f) + N_{\ell}(f) \right)^2 \right], \quad (12)$$

where  $N_{\ell}$  is the uncertainties in the measurement of  $C_{\ell}^{\text{GWGW}}(f)$  due to timing residual noise,  $f_{\text{sky}}$  denotes the fraction of the sky covered by the galaxy catalog. For LSST,  $f_{\text{sky}} = 0.42$ , and we assume the same value throughout the rest of this paper.

In Fig. 2, we show the  $C_{\ell}^{\text{GWGW}}(f)$  as a function of frequency, obtained for the LSST-like galaxy surveys. The overall shape of the spectrum is relatively insensitive to variations in the population model. The case with a large value of  $\eta$  requires a relatively smaller number of sources to generate the same power spectrum. Hence, in this scenario, the anisotropy is expected to be larger, as evident from the figure. Similarly, the case where heavier BHs reside at higher redshifts (positive  $\nu$ ) results in a higher amplitude compared to the scenario with lighter BHs at higher redshifts, due to the same underlying reason as the previous case. In the cases, with more negative  $\alpha$  and small  $\lambda$ , more BHs are emitting at low frequencies. Hence, the curve for the case of  $\alpha = -3.6$  is above the  $\alpha = -2.6$  at high frequencies and below  $\alpha = -2.6$  at low frequencies.

The angular cross-correlation between the SGWB map and the galaxy map can be defined as (Sah & Mukherjee 2024)

$$\begin{aligned} C_{\ell}^{\text{gGW}}(f) &\equiv \langle c_{\ell m}^{\text{GW}}(f) c_{\ell m}^{\text{g}} \rangle, \\ &= \frac{2}{\pi} \int dz_1 b_g(z_1) \phi_g(z_1) D(z_1) \int dz_2 b_g(z_2) \phi_{\text{GW}}(f, z_2) \\ &\quad \times D(z_2) \int k^2 dk j_{\ell}(kr(z_1)) j_{\ell}(kr(z_2)) P(k), \end{aligned} \quad (13)$$

where  $j_{\ell}(kr)$  are spherical Bessel functions of order  $\ell$ , and  $P(k)$  is the matter power spectrum at redshift  $z=0$ . The term  $D(z)$  represents the growth factor of density perturbations over time,  $\phi_g(z) \equiv \frac{\frac{dn}{dz}}{\int \frac{dn}{dz} dz}$  is the galaxy window function. The cross-correlation can also be obtained between the individual tomographic bin and the frequency bin of the SGWB density

$$C_{\ell}^{\text{gGW}}(f, z) \equiv \langle c_{\ell m}^{\text{GW}}(f) c_{\ell m}^{\text{g}}(z) \rangle, \quad (14)$$

where  $C_{\ell}^{\text{gGW}}(f, z)$  is the cross power spectrum between SGWB density measured in a frequency bin ( $\Delta f$ ) around the frequency  $f$  and the galaxy in a redshift bin ( $\Delta z$ ) around  $z$ ,  $c_{\ell m}^{\text{g}}(z)$  is the spherical harmonic component of the galaxy number density in a redshift bin around  $z$ . The uncertainty in the measurement of the  $C_{\ell}^{\text{gGW}}(f, z)$  signal,  $\Sigma_{\text{gGW}}^2(f, \ell, z)$ ,

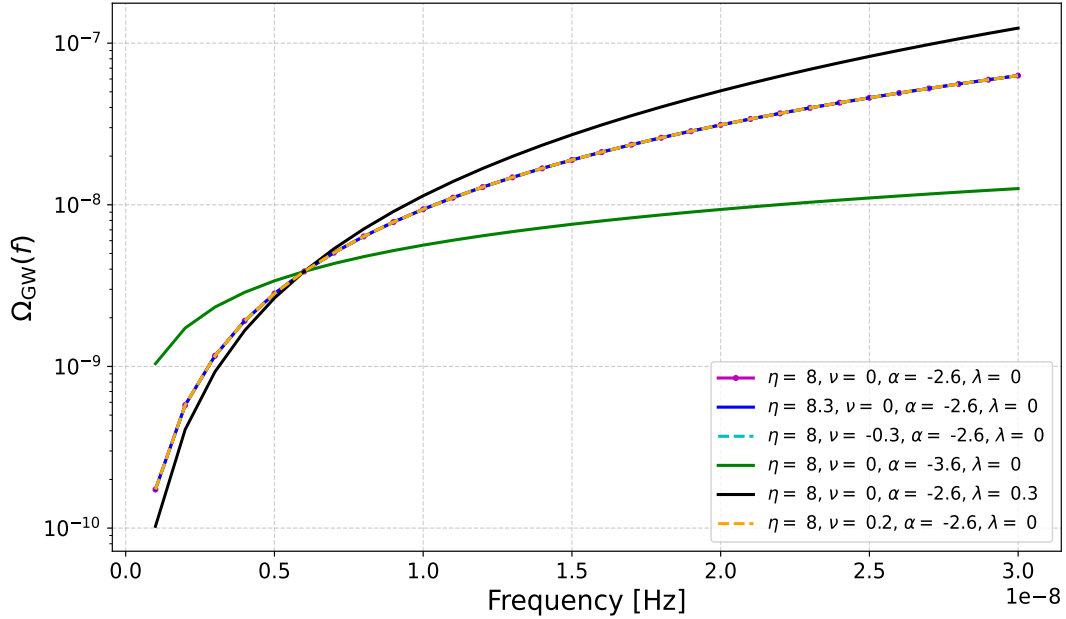


**Figure 1.** The SGWB energy density spectrum,  $\Omega_{\text{GW}}(f)$ , as a function of frequency for different SMBHB population models. Various population parameters influence the spectrum differently:  $\eta$  and  $\nu$  primarily determine the overall amplitude, while  $\alpha$  and  $\lambda$  shape the spectral form.

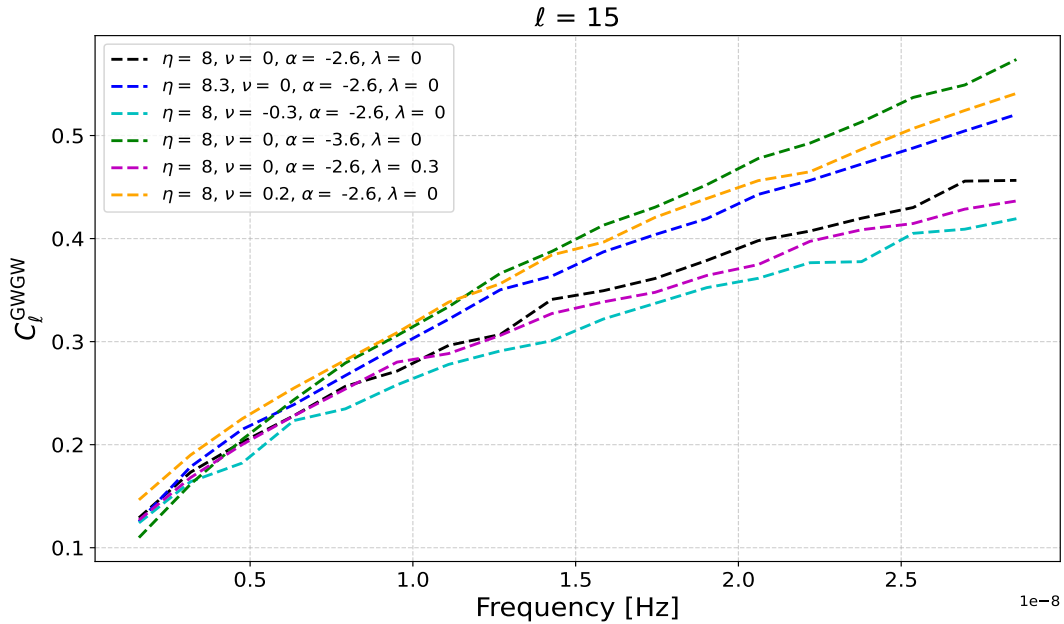


**Figure 2.** The angular power spectrum of SGWB density,  $C_{\ell}^{\text{GWGW}}(f)$  at  $\ell = 15$ , as a function of frequency for different SMBHB population models. The  $C_{\ell}^{\text{GWGW}}(f)$  signal is expected to be shot noise-dominated, leading to a flat spectrum in spherical harmonic mode  $\ell$ . The overall spectrum remains largely unaffected by the population model.

in the Gaussian limit is given by

$$\Sigma_{\text{gGW}}^2(f, \ell, z) = \frac{1}{f_{\text{sky}}(2\ell + 1)} \left[ (C_{\ell}^{\text{gGW}}(f, z))^2 + (C_{\ell}^{\text{gg}}(z) + \frac{1}{n_{\text{g}}})(C_{\ell}^{\text{GWGW}}(f) + N_{\ell}(f)) \right], \quad (15)$$

where  $C_{\ell}^{\text{GWGW}}$  and  $C_{\ell}^{\text{gg}}$  represent the angular power spectra

of SGWB and galaxy, respectively. The term  $n_{\text{g}}$  corresponds to the mean galaxy number per steradian.

In Fig. 3, we illustrate the cross-correlation signal,  $C_{\ell}^{\text{gGW}}(f)$ , between SGWB (at  $f = 6 \times 10^{-9}$  Hz) and galaxy distribution (redshift integrated galaxy map) of LSST-like surveys, for different values of  $\eta$ ,  $\nu$ ,  $\alpha$ , and  $\lambda$ . The  $C_{\ell}^{\text{gGW}}(f)$  spectrum depends on the relative contribution of the SGWB and the galaxy density from different

redshifts. The  $C_\ell^{\text{gGW}}(f)$  is largely unaffected by variations in the  $M_* - M_{\text{BH}}$  relation,  $\eta$ . However, it exhibits significant changes when redshift evolution is incorporated into the  $M_* - M_{\text{BH}}$  ( $\nu \neq 0$ ). For instance, with  $\nu = -0.3$ , the SMBHBs are relatively less massive at high redshifts compared to the low redshifts. This means the relative contribution of the SGWB signal is enhanced at lower redshifts. Similarly, in Fig. 4, we show the  $C_\ell^{\text{gGW}}$  as a function of frequency for  $\ell = 15$ . The curve remains unaffected for all the cases except for the case where  $\lambda \neq 0$ . This is because the window function ( $\phi_{\text{GW}}(f, z)$ ) is independent of the frequency for all cases where the frequency distribution is independent of the redshift.

The angular power spectrum can be interpreted as the projection of the matter power spectrum onto the window function. This implies that if both the window function and the power in the matter power spectrum corresponding to a given  $\ell$ -mode exhibit a similar trend with redshift, the power in that  $\ell$ -mode will be enhanced. The Fourier modes (k-modes) associated with a given angular multipole  $\ell$  decrease with redshift. Under the Limber approximation, they are given by,  $k = \frac{\ell+1/2}{d_m(z)}$ , where  $d_m(z)$  represents the comoving distance. At low  $\ell$  values, this decrease corresponds to a reduction in the clustering power of matter as redshift increases. For negative values of  $\nu$ , where the window function declines more steeply with redshift, the projection factor becomes larger. Consequently, the angular power spectrum  $C_\ell^{\text{gGW}}(f)$  is expected to be larger at low  $\ell$ . However, at higher  $\ell$  values, the increase in redshift corresponds to an increase in the clustering power of matter, thereby reducing the projection factor. As a result, for these higher  $\ell$  values,  $C_\ell^{\text{gGW}}(f)$  decreases as  $\nu$  decreases.

The steepness of the frequency distribution, governed by  $\alpha$  and  $\lambda$ , also affects  $C_\ell^{\text{gGW}}(f)$ . A more negative  $\alpha$  implies a steeper frequency distribution, causing more sources emitting at lower frequencies to be redshifted out of the observational band, decreasing the value of the window function at higher redshifts. This behavior impacts the  $C_\ell^{\text{gGW}}(f)$  spectrum in a manner similar to  $\nu$ , as both parameters influence the relative redshift contributions.

#### 4 MAPPING BETWEEN OBSERVATIONAL QUANTITIES AND PHYSICAL PARAMETERS

The nHz SGWB encodes valuable information about the population and evolution of SMBHBs. The observable quantities, such as the SGWB spectral density  $\Omega_{\text{GW}}(f)$ , the angular power spectrum  $C_\ell^{\text{gGW}}(f)$ , and the cross-angular power spectrum  $C_\ell^{\text{gGW}}(f)$ , exhibit variations in amplitude and shape across spatial ( $\ell$ ) and spectral ( $f$ ) frequencies. These variations are governed by underlying physical parameters, including the SMBHB mass distribution ( $\eta, \rho, \nu$ ), and the parameters controlling the frequency distribution of the GW sources ( $\alpha, \lambda$ ). Understanding the dependence of these observables on the physical parameters is crucial for determining which aspects of the SMBHB population can be constrained from PTA observations. In this section, we examine how these parameters affect the observed signals and discuss their implications for constraining the SMBHB population. We particularly focus on the  $\Omega_{\text{GW}}(f)$  and  $C_\ell^{\text{gGW}}(f)$

in this section, as these two mainly contribute in the constraining the physical parameters we are interested in this analysis.

(i) **Impact of Physical Parameters on  $\Omega_{\text{GW}}(f)$ :** The slope of the  $\Omega_{\text{GW}}(f)$  curve may deviate from a simple power law due to the redshift evolution of the frequency distribution. To account for this, we fit a power law to  $\Omega_{\text{GW}}$ , parameterized by an amplitude  $Amp$ , a transition frequency  $f_t$ , and two spectral indices  $\beta_1$  and  $\beta_2$ , such that

$$\log_{10}(\Omega_{\text{GW}}(f)) \equiv \begin{cases} Amp + \beta_1(\log_{10}(f/f_t)), & f \leq f_t, \\ Amp + \beta_2(\log_{10}(f/f_t)), & f > f_t \end{cases} \quad (16)$$

These parameters are the observable quantities that can demonstrate the observed features in the SGWB power spectra. In Fig. 5, we show how the observable quantities namely,  $Amp, \beta_1, \beta_2$  and  $f_t$ , is affected by the physical parameters like  $\eta, \nu, \alpha$ , and  $\lambda$ . We adopt the fiducial values  $\eta = 8, \rho = 1, \nu = -0.3, \alpha = -2.6$ , and  $\lambda = 0.3$ , and vary each physical parameter one at a time to study its impact on the observables. The effects of different physical parameters on these features are summarized below.

- **Overall Amplitude ( $Amp$ ) and Transition Frequency ( $f_t$ ):** Since we have normalized  $\Omega_{\text{GW}}(f)$  such that it remains fixed at a reference frequency ( $f_{\text{ref}} = 6 \times 10^{-9}$  Hz),  $Amp$  and  $f_t$  is unaffected by variations in  $\eta$ . However, it is strongly influenced by the frequency distribution parameters,  $\alpha$ , and  $\lambda$ , both of which lead to an increase in  $Amp$  as their values increase. A positive value of  $\nu$  increases the contribution from high-redshift sources, where the frequency distribution is shallower. As a result, the spectrum becomes steeper, shifting  $f_t$  to a lower value and consequently, decreasing  $Amp$ .
- **Spectral Slopes ( $\beta_1, \beta_2$ ):** The positive change in both  $\alpha$  and  $\lambda$  results in the steeper  $\Omega_{\text{GW}}(f)$ , as a result both  $\beta_1$  and  $\beta_2$  increase with the increase in  $\alpha$  and  $\lambda$ . The parameters  $\nu$  do not affect the spectral slope of the  $\Omega_{\text{GW}}(f)$  significantly.

These findings indicate that the spectral shape of  $\Omega_{\text{GW}}(f)$  is mostly insensitive to the parameter  $\eta$  and there exists significant degeneracy between  $\eta$  and  $\nu$ . However,  $\Omega_{\text{GW}}(f)$  shows that spectral features are strongly affected by changes in  $\alpha$  and  $\lambda$ . This implies that  $\Omega_{\text{GW}}(f)$  can effectively constrain the frequency evolution of SMBHB.

(ii) **Impact of Physical Parameters on  $C_\ell^{\text{gGW}}(f)$ :** Similarly, we fit the cross-correlation spectrum  $C_\ell^{\text{gGW}}(f)$  at a fixed frequency ( $6 \times 10^{-9}$  Hz) using a Gaussian model.

$$C_\ell^{\text{gGW}} \equiv A_p \exp\left(\frac{-(\ell - \ell_p)^2}{2\sigma_{L,R}^2}\right), \quad (17)$$

where,  $\ell_p$  is the multipole where  $C_\ell^{\text{gGW}}$  peaks,  $A_p$  is the peak amplitude,  $\sigma_L$ , and  $\sigma_R$  are the standard deviations of the one-sided Gaussian fitted to the left and right of the peak, respectively. For fitting, we select five consecutive points around the peak. We denote the amplitude of  $C_\ell^{\text{gGW}}$  at  $\ell = \ell_p$  by  $A_p$ . In Fig. 6, we demonstrate how the structure of the  $C_\ell^{\text{gGW}}$  is impacted by the physical parameters. We adopt fiducial values of  $\eta = 8, \rho = 1, \nu = -0.3, \alpha = -2.6$ , and  $\lambda = 0.3$ , and vary one parameter at a time

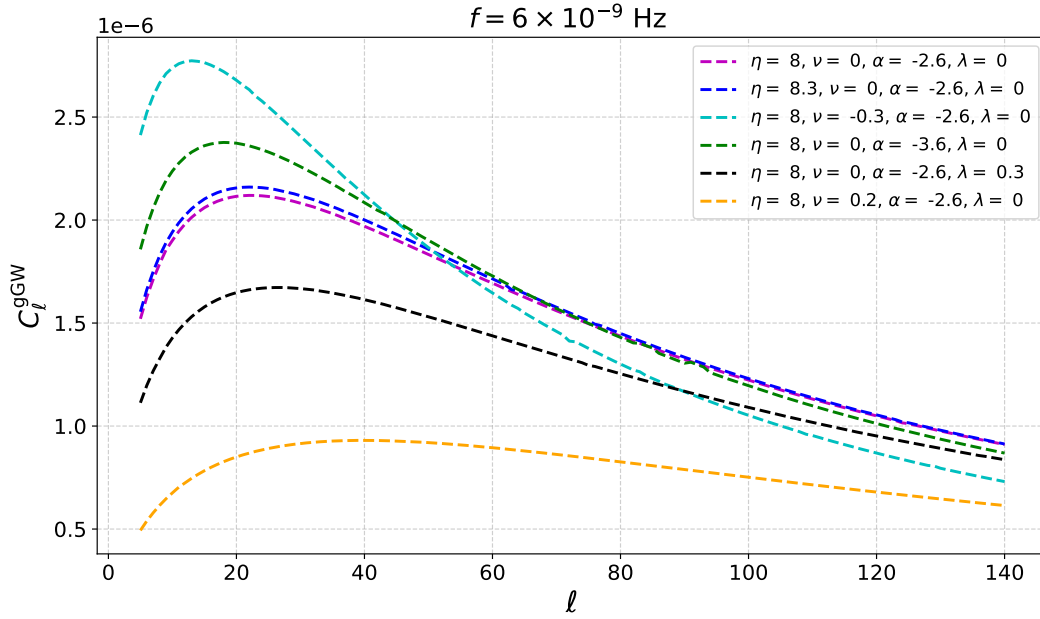


**Figure 3.** The cross-correlation power spectrum between SGWB density and the galaxy distribution,  $C_\ell^{\text{gGW}}$ , as a function of spherical harmonic mode  $\ell$  at a GW frequency of  $6\text{e-}9$  Hz, for different population models. The shape and structure of the signal are primarily influenced by the population parameters  $\nu$ ,  $\alpha$ , and  $\lambda$ , while  $\eta$ , which controls the overall amplitude of  $\Omega_{\text{GW}}(f)$ , has little to no effect on  $C_\ell^{\text{gGW}}$ .

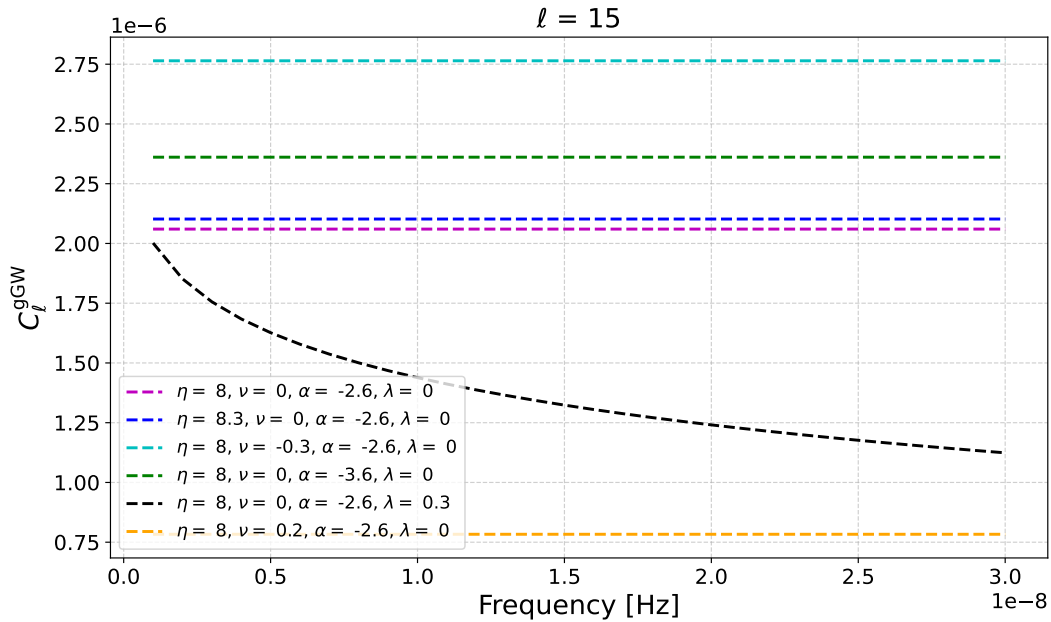


**Figure 4.** The cross-correlation power spectrum between SGWB density and the galaxy distribution,  $C_\ell^{\text{gGW}}$  at  $\ell = 15$ , as a function of GW frequency for different population models. The curve remains unchanged across all scenarios except when  $\lambda \neq 0$ . This is because the window function  $\phi_{\text{GW}}(f, z)$  is independent of frequency in cases where the frequency distribution does not depend on redshift.

while keeping the others fixed. The effects of different physical parameters on these features are summarized below.

- *Peak Location ( $\ell_p$ ):* As expected from earlier discussions, the parameter  $\eta$  has a negligible effect on the cross-correlation features. In contrast,  $\nu$  has a significant impact, shifting  $\ell_p$  to higher values as  $\nu$  increases. This shift

occurs because a higher  $\nu$  reduces the relative contribution from lower redshifts and increases the power in higher  $\ell$  modes, as discussed in Sec. 3. The impact of  $\alpha$  and  $\lambda$  on  $\ell_p$  is relatively small. However,  $\ell_p$  shifts toward higher values with an increase in both parameters. This occurs because the frequency distribution becomes shallower as these parameters increase, resulting in fewer sources being

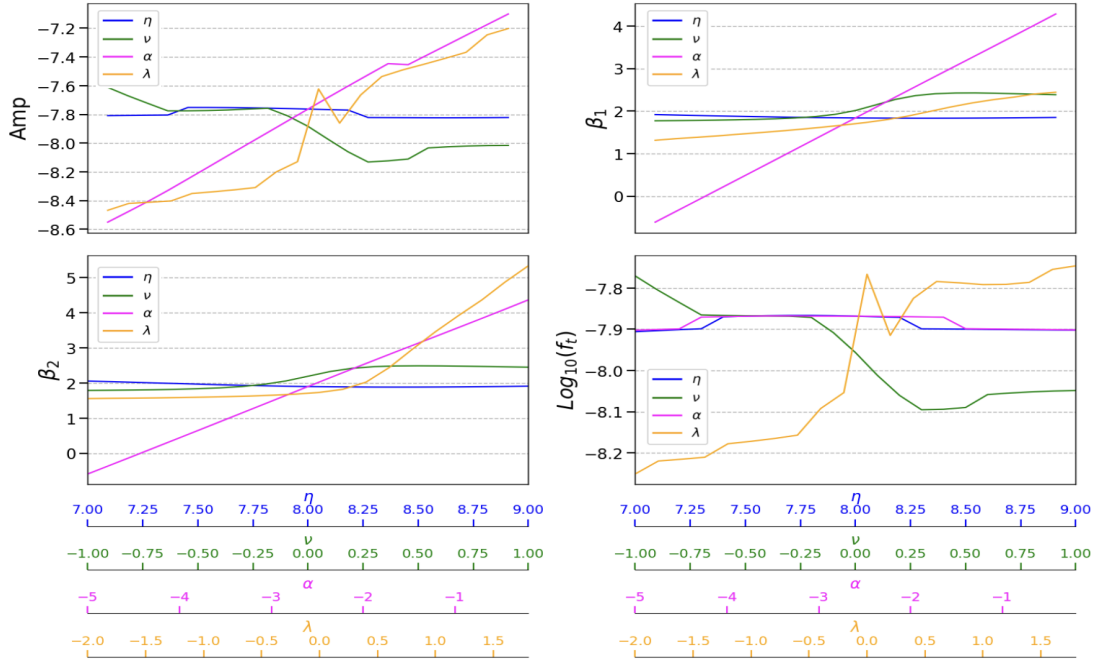


**Figure 5.** Mapping between the SGWB power spectrum ( $\Omega_{\text{GW}}(f)$ ) features and physical parameter,  $\eta$ ,  $\nu$ ,  $\alpha$  and  $\lambda$ . The  $\log_{10}(\Omega_{\text{GW}}(f))$  is fitted to linear curve with an intercept  $Amp$  and slopes  $\beta_1$  and  $\beta_2$  with a parameters  $f_t$  denoting the transition frequency of the curve from slope  $\beta_1$  to  $\beta_2$ .

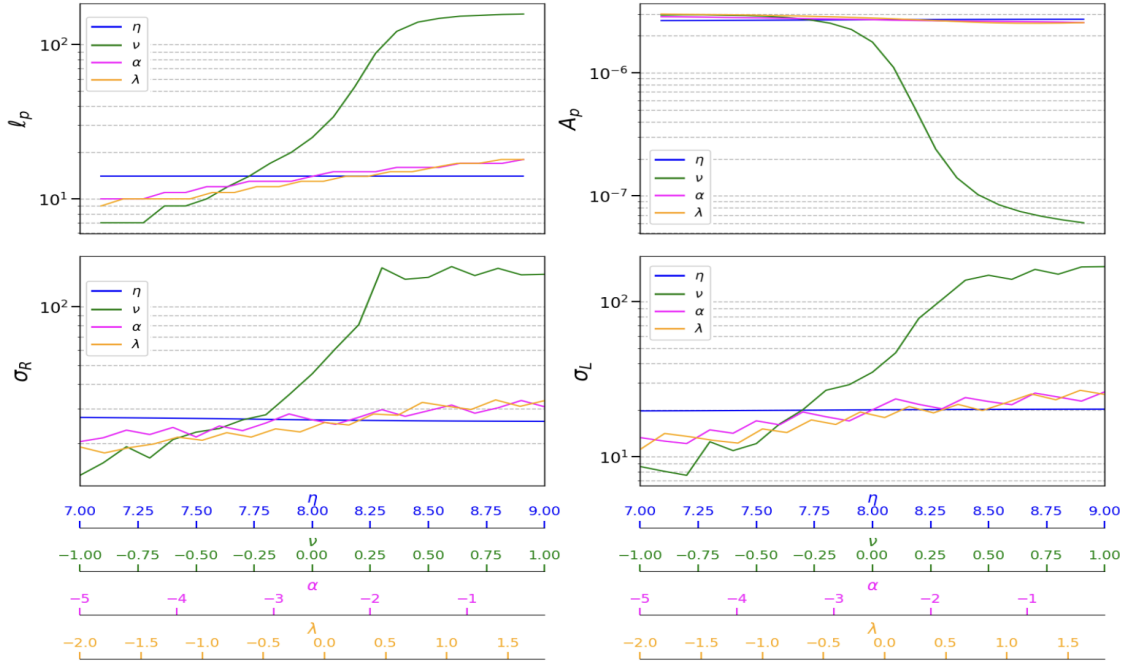


**Figure 6.** Mapping between the cross-angular power spectrum ( $C_\ell^{\text{gGW}}$ ), at frequency  $6 \times 10^{-9}$  Hz. The  $C_\ell^{\text{gGW}}$  is fitted with one-sided Gaussian to the left and right sides of the peak of  $C_\ell^{\text{gGW}}$ . The  $\ell_p$  denotes the  $\ell$  value at which  $C_\ell^{\text{gGW}}$  peaks,  $A_p$  is the height of the peak, and  $\sigma_R$  and  $\sigma_L$  are the standard deviation of the left and right Gaussian.

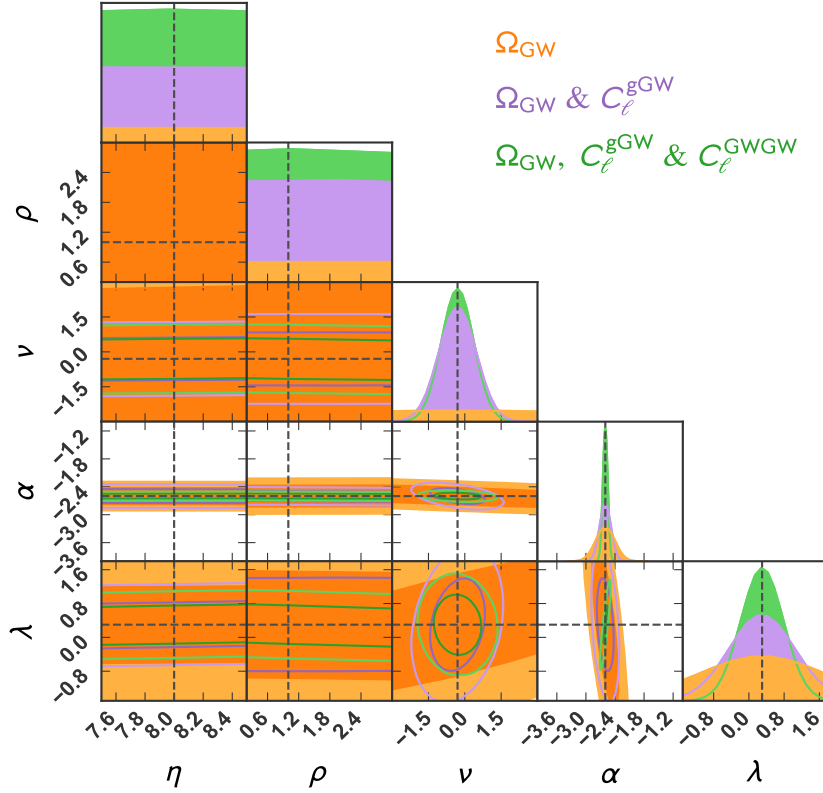


**Figure 7.** Corner plot showing the constraints on the parameters  $\eta$ ,  $\nu$ ,  $\alpha$ , and  $\lambda$  for three scenarios: (i) using only  $\Omega_{\text{GW}}(f)$ , (ii) including  $C_{\ell}^{\text{gGW}}(f)$  in addition to  $\Omega_{\text{GW}}(f)$ , and (iii) combining all three— $\Omega_{\text{GW}}(f)$ ,  $C_{\ell}^{\text{gGW}}(f)$ , and  $C_{\ell}^{\text{gGWGW}}(f)$ . The posterior distributions and the corresponding correlations between parameters are displayed for each case. The constraints are derived for 2000 isotropically distributed pulsars with an equal noise power spectrum. The injected parameter values are  $\eta = 8$ ,  $\nu = -0.3$ ,  $\alpha = -2.6$ , and  $\lambda = 0.3$ .

redshifted out of the observation band. Consequently, the window function attains relatively larger values at higher redshifts compared to a steeper frequency distribution. By the same reasoning as in Sec. 3, the angular power spectrum  $C_{\ell}^{\text{gGW}}$  at lower  $\ell$  values decreases with increasing  $\alpha$  and  $\lambda$ . This implies that  $\ell_p$  shifts to a higher value with the increase in these parameters.

- *Peak Amplitude ( $A_p$ ):* The peak amplitude  $A_p$  decreases as  $\nu$  increases, as the overall amplitude of the SGWB diminishes with an increasing contribution from higher redshifts, as discussed in Sec. 3. The effect of  $\alpha$  and  $\lambda$  on  $A_p$  is relatively weak. By the same reasoning as in the case of  $\ell_p$ , the  $A_p$  increases with these parameters.

- *Peak Width ( $\sigma_L, \sigma_R$ ):* The parameter  $\nu$  strongly influences both  $\sigma_L$  and  $\sigma_R$ , causing them to increase as  $\nu$  increases. This occurs because a larger  $\nu$  spreads the SGWB signal over a broader range of redshifts. Additionally,  $\sigma_L$  and  $\sigma_R$  increase with  $\alpha$  and  $\lambda$ , as a shallower frequency distribution implies a significant contribution from higher-redshift sources. Consequently, the  $C_{\ell}^{\text{gGW}}$  decreases less steeply with  $\ell$ .

These results demonstrate that  $\nu$  is the key parameter influencing the cross-correlation power spectrum, highlighting the crucial role of  $C_{\ell}^{\text{gGW}}$  in breaking the degeneracy

present in  $\Omega_{\text{GW}}(f)$  among  $\eta$ ,  $\rho$ , and  $\nu$ . While both  $\Omega_{\text{GW}}(f)$  and  $C_{\ell}^{\text{gGW}}$  are sensitive to  $\alpha$  and  $\lambda$ , these parameters exhibit some degeneracy in both signals individually. However, their combination significantly improves constraints, providing more precise measurements of these quantities.

## 5 CROSS-CORRELATION ANALYSIS IN PULSAR TIMING ARRAYS

PTAs are uniquely capable of detecting the SGWB by correlating the timing residuals of multiple millisecond pulsars. These residuals are influenced by passing GWs, which induce correlated deviations in the pulse arrival times. The cross-correlation of these timing residuals provides a powerful tool to probe GW signals and differentiate them from uncorrelated noise sources.

The timing residual in the timing signal of a pulsar located in the direction  $\hat{p}$  due to the GW propagating in the direction  $\hat{n}$  is given by (Anholm et al. 2009; Chamberlin et al. 2015; Hobbs & Dai 2017; Burke-Spolaor et al. 2019;



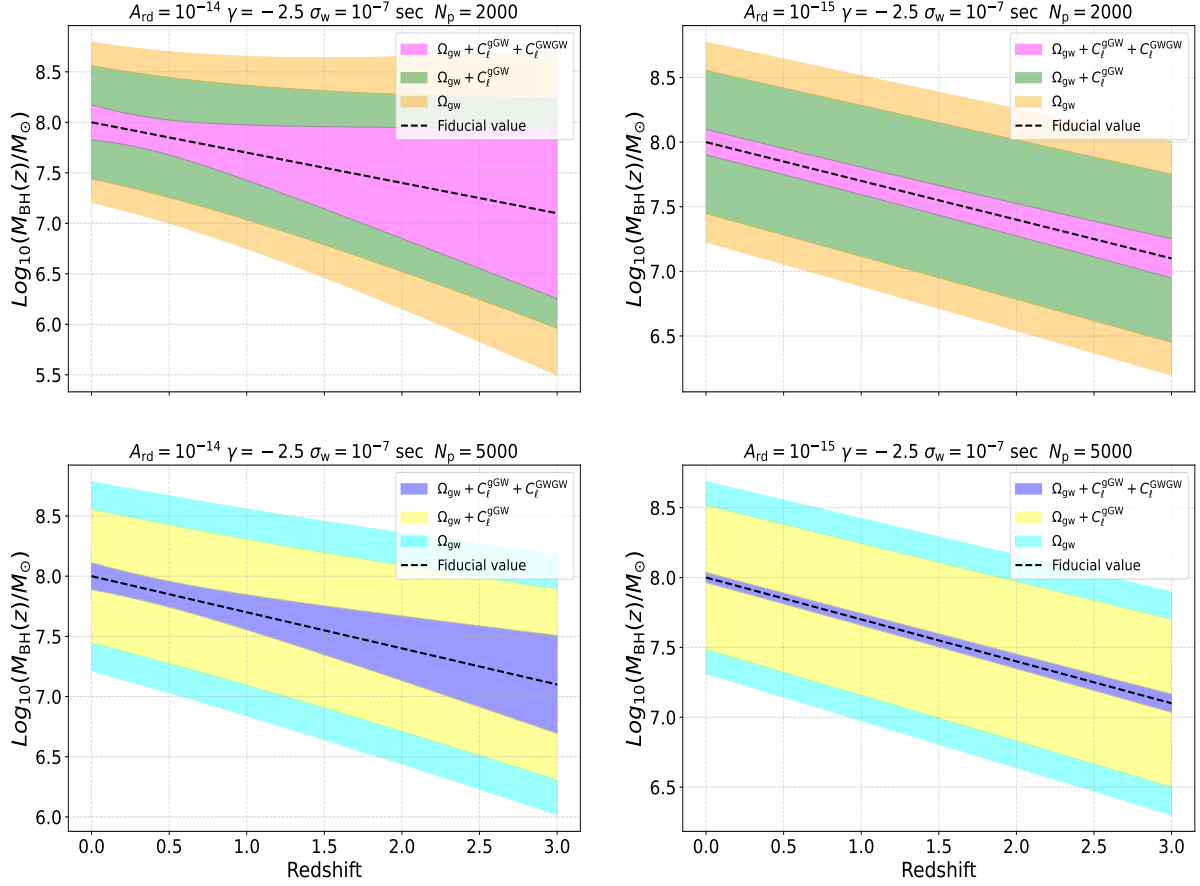


**Figure 8.** Evolution of the mean mass of the SMBHB,  $M_{\text{BH}}(z)$ , given by Eq. (4), for a stellar mass of  $M_* = 10^{11} M_\odot$  as a function of redshift. The shaded regions represent the 68% credible interval on  $M_{\text{BH}}$ . The results are shown for two different PTA noise configurations: (i)  $A_{\text{rd}} = 10^{-14}$ ,  $\gamma = -2.5$ ,  $\sigma_w = 10^{-7}$  sec (left panel) and (ii)  $A_{\text{rd}} = 10^{-15}$ ,  $\gamma = -2.5$ ,  $\sigma_w = 10^{-7}$  sec (right panel). Each configuration is analyzed for  $N_p = 2000$  (upper panel) and  $N_p = 5000$  (lower panel) pulsars. The injected parameter values are  $\eta = 8$ ,  $\nu = -0.3$ ,  $\alpha = -2.6$ , and  $\lambda = 0.3$ . A Gaussian prior is applied to  $\eta$  and  $\rho$ , with a standard deviation of 10% of their injected values. The results are presented for three cases: (1) considering only  $\Omega_{\text{GW}}$ , (2) including both  $\Omega_{\text{GW}}$  and  $C_\ell^{\text{gGW}}$ , and (3) incorporating  $\Omega_{\text{GW}}$ ,  $C_\ell^{\text{gGW}}$ , and  $C_\ell^{\text{gGWG}}$ .

(Maiorano et al. 2021)

$$r(t) = \int_0^t dt' \int_{S^2} d\hat{n} \frac{1}{2} \frac{\hat{p}_i \hat{p}_j}{1 + \hat{n} \cdot \hat{p}} \left( h_{ij}(t', \hat{n}) - h_{ij}(t' - t_p, \hat{n}) \right), \quad (18)$$

where  $h_{ij}$  is the metric perturbation,  $t_p$  is the light travel time between the pulsar and the earth. The metric perturbation from an SGWB can be expanded as:

$$h_{ij}(t, \hat{n}) = \sum_A \int d\hat{n} \int_{-\infty}^{\infty} df h_A(f, \hat{n}) e^{i2\pi f(t - \hat{n} \cdot \mathbf{x})} e_{ij}^A(\hat{n}), \quad (19)$$

where  $A = +, \times$  denotes the polarization modes and  $e_{ij}^A(\hat{n})$  are the polarization tensors.

This expansion allows us to express the timing residuals in the frequency domain

$$\tilde{r}(f, \hat{n}) = \frac{1}{2\pi i f} \left( 1 - e^{-2\pi i f L(1 + \hat{n} \cdot \hat{p})} \right) \sum_A h_A(f, \hat{n}) \mathcal{F}^A(\hat{p}, \hat{n}), \quad (20)$$

The expectation value of the metric perturbation,  $\langle h_A^*(f, \hat{n}) h_A(f', \hat{n}') \rangle$  can be expressed as a function of strain spectral density,  $S_h(f, \hat{n})$

$$\langle h_A^*(f, \hat{n}) h_A(f', \hat{n}') \rangle = \delta(f - f') \delta^2(\hat{n} - \hat{n}') \frac{1}{16\pi} S_h(f, \hat{n}). \quad (21)$$

Using Eq. (20) and Eq. (21), we can express the cross-correlation of the Fourier transform of timing residuals between two pulsars, denoted by I and J as

$$\begin{aligned} \langle \tilde{r}_I(f) \tilde{r}_J(f') \rangle &= \frac{1}{24\pi^2} \delta(f - f') f^{-2} \int S_h(f, \hat{n}) \Gamma_{IJ}(\hat{n}) d\hat{n}, \\ &= \frac{1}{24\pi^2} \delta(f - f') f^{-2} S_h(f) \int P(f, \hat{n}) \Gamma_{IJ}(\hat{n}) d\hat{n}, \end{aligned} \quad (22)$$

where  $S_h(f, \hat{n}) \equiv S_h(f) P(f, \hat{n})$ , and  $S_h(f) \equiv \int_{S^2} d\hat{n} S_h(f, \hat{n})$ .

The spectral density,  $S_h(f)$  can be written in terms of the characteristic strain ( $h_c(f)$ ) and  $\Omega_{\text{GW}}(f)$

$$h_c^2(f) = f S_h(f), \quad (23)$$

$$\Omega_{\text{GW}}(f) = \frac{2\pi^2}{3H_0^2} f^3 S_h(f). \quad (24)$$

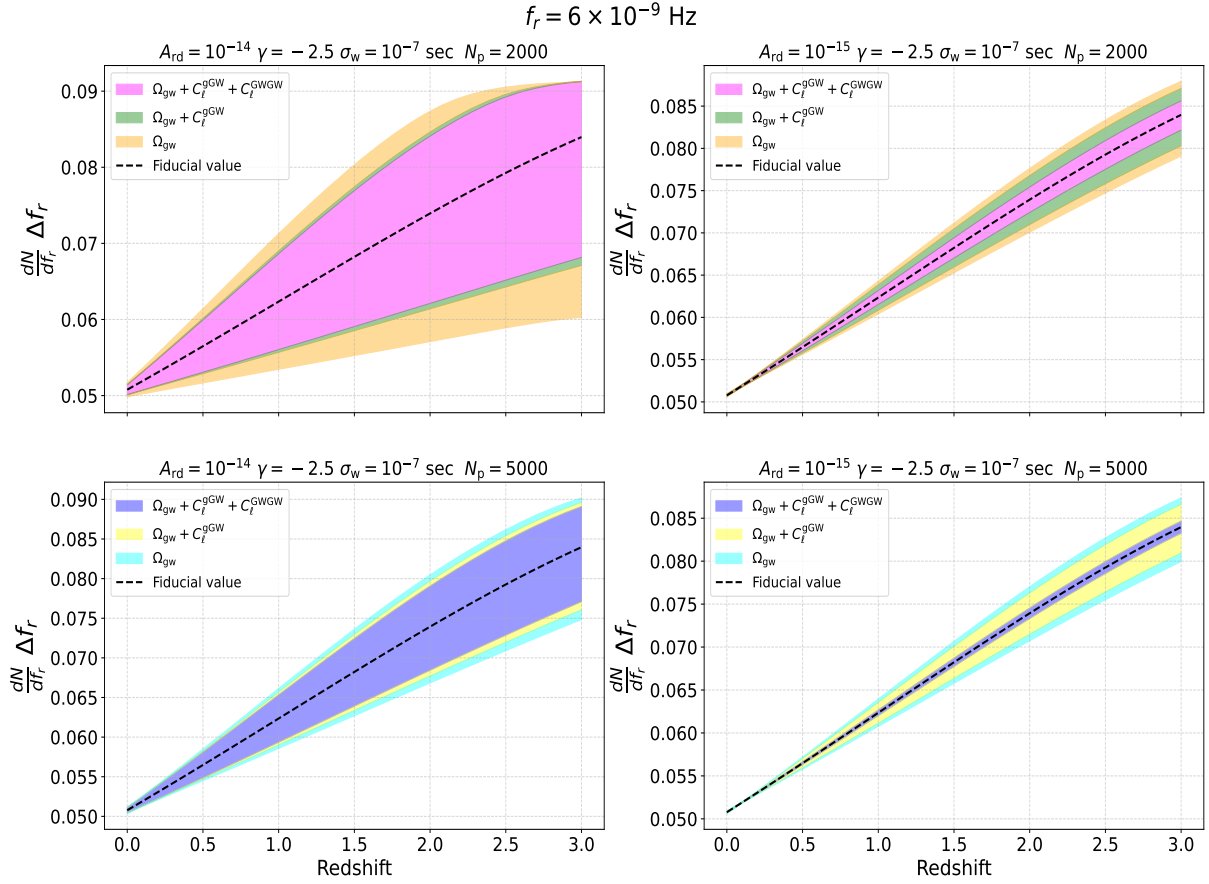


**Figure 9.** Redshift evolution of the frequency distribution, normalized  $\frac{dN}{df_r} \times \Delta f_r$  at  $f_r = 6 \times 10^{-9}$  Hz, of SMBHBs as a function of redshift. The shaded regions represent the 68% credible interval. Results are shown for two different PTA noise configurations: (i)  $A_{\text{rd}} = 10^{-14}$ ,  $\gamma = -2.5$ ,  $\sigma_w = 10^{-7}$  sec (left panel) and (ii)  $A_{\text{rd}} = 10^{-15}$ ,  $\gamma = -2.5$ ,  $\sigma_w = 10^{-7}$  sec (right panel). Each configuration is analyzed for  $N_p = 2000$  (upper panel) and  $N_p = 5000$  (lower panel) pulsars. The injected parameter values are  $\eta = 8$ ,  $\nu = -0.3$ ,  $\alpha = -2.6$ , and  $\lambda = 0.3$ . A Gaussian prior is applied to  $\eta$  and  $\rho$ , with a standard deviation of 10% of their injected values. The results are presented for three cases: (1) considering only  $\Omega_{\text{GW}}$ , (2) including both  $\Omega_{\text{GW}}$  and  $C_\ell^{\text{gGW}}$ , and (3) incorporating  $\Omega_{\text{GW}}$ ,  $C_\ell^{\text{gGW}}$ , and  $C_\ell^{\text{GWGW}}$ .

In addition to the GW signal, timing residuals contain uncorrelated noise contributions. The timing residual noise power spectrum can be modeled as

$$P(f) = P_w(f) + P_r(f), \quad (25)$$

where  $P_w(f) = 2 \Delta t \sigma_w^2$  is the white noise. Here,  $\Delta t$  denotes the cadence of the pulsar time-of-arrival (TOA) measurements, and  $\sigma_w$  represents the uncertainty in the TOA measurements.  $P_r(f)$  is the red-noise power spectrum which is composed of two components:  $P_1(f)$ , the intrinsic red noise, and  $P_{\text{gw}}(f)$ , the GW-induced noise

$$P_r(f) = P_1(f) + P_{\text{gw}}(f). \quad (26)$$

The intrinsic red noise,  $P_1(f)$ , is modeled as

$$P_1(f) = \frac{A_{\text{rd}}^2}{12\pi^2} \left( \frac{f}{f_{1\text{yr}}} \right)^\gamma f_{1\text{yr}}^{-3}, \quad (27)$$

where  $A_{\text{rd}}$  is the amplitude of the intrinsic red noise,  $f_{1\text{yr}}$  is the reference frequency corresponding to one year,  $f_{1\text{yr}} = 1/\text{yr}$ , and  $\gamma$  is the spectral index of the red noise. The GW-

induced noise is expressed as:

$$P_{\text{gw}}(f) = \frac{h_c^2}{12\pi^2} f^{-3}, \quad (28)$$

where  $h_c$  is the characteristic strain of the GW background. This formulation provides a comprehensive decomposition of the total power spectrum into white noise and red noise components, enabling the modeling of both instrumental effects and astrophysical contributions to the timing residuals.

In addition to the white noise and red noise components discussed above, other potential sources of noise can impact pulsar timing residuals. These include lensing noise, which arises due to the gravitational lensing of pulsar signals by intervening massive structures, and pulsar glitch noise, which results from sudden changes in the rotational frequency of pulsars (Lower et al. 2020; Goncharov et al. 2021; Reardon et al. 2023; Falxa et al. 2024; Di Marco et al. 2024). Lensing noise can introduce frequency-dependent distortions in the timing residuals, while pulsar glitches are typically analyzed on an individual pulsar basis, as their effects are highly specific to each pulsar's internal dynamics. In this analysis, these noise sources are not included, as their contributions

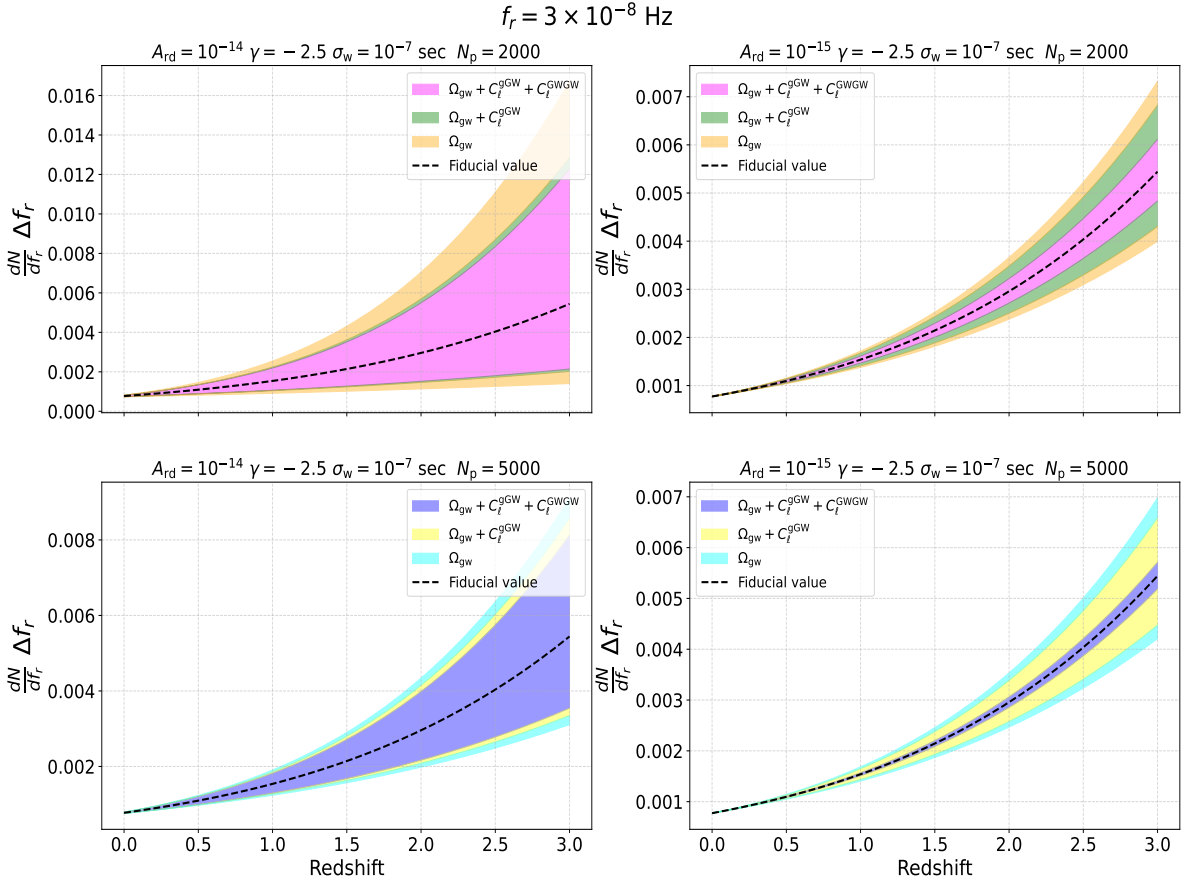


**Figure 10.** Redshift evolution of the frequency distribution, normalized  $\frac{dN}{df_r} \times \Delta f_r$  at  $f_r = 3 \times 10^{-8}$  Hz, of SMBHBs as a function of redshift. The shaded regions represent the 68% credible interval. Results are shown for two different PTA noise configurations: (i)  $A_{\text{rd}} = 10^{-14}$ ,  $\gamma = -2.5$ ,  $\sigma_w = 10^{-7}$  sec (left panel) and (ii)  $A_{\text{rd}} = 10^{-15}$ ,  $\gamma = -2.5$ ,  $\sigma_w = 10^{-7}$  sec (right panel). Each configuration is analyzed for  $N_p = 2000$  (upper panel) and  $N_p = 5000$  (lower panel) pulsars. The injected parameter values are  $\eta = 8$ ,  $\nu = -0.3$ ,  $\alpha = -2.6$ , and  $\lambda = 0.3$ . A Gaussian prior is applied to  $\eta$  and  $\rho$ , with a standard deviation of 10% of their injected values. The results are presented for three cases: (1) considering only  $\Omega_{\text{GW}}$ , (2) including both  $\Omega_{\text{GW}}$  and  $C_\ell^{\text{gGW}}$ , and (3) incorporating  $\Omega_{\text{GW}}$ ,  $C_\ell^{\text{gGW}}$ , and  $C_\ell^{\text{gGWG}}$ .

are expected to be subdominant compared to the dominant white and red noise and GW-induced noise at the frequencies of interest. However, future work will incorporate these additional noise sources to provide a more comprehensive characterization of the timing residuals and their impact on SGWB detection.

## 6 FISHER FORECAST FOR CONSTRAINING THE PHYSICAL PARAMETERS

Unlike individually resolved sources, the SGWB represents a stochastic superposition of numerous unresolved binary signals. The power spectral density of SGWB and its anisotropy encodes information about the population of the binaries and its cosmic evolution. Given the computational cost of modeling the SGWB signal, we perform a Fisher analysis to show how well the SGWB and the angular power spectrum can constrain the properties of the SMBHB population and its evolution with redshift. The Fisher matrix formalism is a widely used statistical technique for estimating the precision with which model parameters can be deter-

mined from observational data (Fisher 1935; Tegmark et al. 1997). This approach is particularly effective in scenarios where the likelihood function is well-approximated by a multivariate Gaussian. The Fisher information matrix is defined as:

$$F_{ij} = \left\langle \frac{\partial^2 \mathcal{L}}{\partial \theta_i \partial \theta_j} \right\rangle, \quad (29)$$

where  $\mathcal{L} = -\ln L$ , and  $L$  represents the likelihood function. The parameters  $\theta_i$  and  $\theta_j$  are the model parameters being estimated. The Fisher matrix quantifies the amount of information that the data provides about these parameters. The diagonal elements of the inverse of the Fisher matrix ( $F^{-1}$ ) describe the information in the data to individual parameter  $\theta_i$ , while the off-diagonal elements capture the correlations between different parameters. The Cramér-Rao (Rao 1945; Cramér 1946) bound provides a theoretical lower limit on the uncertainty of parameter estimation, given by

$$\Delta \theta_i \geq \sqrt{(F^{-1})_{ii}}. \quad (30)$$

The Cramer-Rao bound estimates the minimum error on the parameters, and does not capture the correlation between the parameters, beyond the Gaussian distribution. However, this demonstrates the scope of this technique is discovering the SMBHBs evolution in the Universe from future observations. Our future work will demonstrate the capability of this technique in a Bayesian framework.

The log-likelihood  $\mathcal{L} \equiv -\ln L$  can be written as

$$\mathcal{L} = \mathcal{L}_{\text{GW}} + \mathcal{L}_{\text{GWGW}} + \mathcal{L}_{\text{gGW}}, \quad (31)$$

where

$$\mathcal{L}_{\text{GW}} \propto \sum_f \frac{(\hat{\Omega}_{\text{GW}}(f) - \Omega_{\text{GW}}(f, \Theta))^2}{2 \Sigma_{\text{GW}}^2(f, \Theta)}, \quad (32)$$

where  $\mathcal{L}_{\text{gGW}}$  represents the likelihood of the  $\hat{\Omega}_{\text{GW}}(f)$  given a set of model parameter  $\Theta$ , and  $\Sigma_{\text{GW}}(f, \Theta)$  is the uncertainty in the measurement of the  $\Omega_{\text{GW}}(f, \Theta)$ .

$$\mathcal{L}_{\text{GWGW}} \propto \sum_{f, \ell} \frac{(\hat{C}_{\ell}^{\text{GWGW}}(f) - C_{\ell}^{\text{GWGW}}(f, \Theta))^2}{2 \Sigma_{\text{GWGW}}^2(f, \ell, \Theta)}, \quad (33)$$

where  $\mathcal{L}_{\text{GWGW}}$  represents the likelihood of the  $\hat{C}_{\ell}^{\text{GWGW}}(f)$  given a set of model parameter  $\Theta$ , and  $\Sigma_{\text{GWGW}}(f, \ell, \Theta)$  is the uncertainty in the measurement of the  $C_{\ell}^{\text{GWGW}}(f, \Theta)$ , and

$$\mathcal{L}_{\text{gGW}} \propto \sum_{f, \ell, z} \frac{(\hat{C}_{\ell}^{\text{gGW}}(f, z) - C_{\ell}^{\text{gGW}}(f, z, \Theta))^2}{2 \Sigma_{\text{gGW}}^2(f, \ell, z, \Theta)}, \quad (34)$$

where  $\mathcal{L}_{\text{gGW}}$  represents the likelihood of the  $\hat{C}_{\ell}^{\text{gGW}}(f, z)$  given a set of model parameter  $\Theta$ , and  $\Sigma_{\text{gGW}}(f, \ell, z, \Theta)$  is the uncertainty in the measurement of the  $C_{\ell}^{\text{gGW}}(f, z, \Theta)$ .

The analysis assumes Gaussian noise for computational simplicity. In reality, the noise may exhibit non-Gaussian features and future studies will explore this aspect. We calculate the  $\Omega_{\text{GW}}(f)$  and  $C_{\ell}^{\text{gGW}}(f)$  signal using the Eq. (1) and Eq. (13), respectively. The estimates from simulations match well with the analytical results. Whereas the  $C_{\ell}^{\text{GWGW}}(f)$  is obtained by averaging the signal over 1000 GW source population realizations using Eq. (11). The  $C_{\ell}^{\text{GWGW}}$  spectrum is dominated by shot noise arising from the stochastic distribution of a finite number of SMBHB sources, requiring statistical averaging over multiple realizations. Simulations are essential in this context, as they capture the variance due to a finite number of sources that are not adequately described by purely analytical approaches.

The uncertainty in the measurement of these quantities is obtained by using the white and red noise expressions as described in Sec. 5. The uncertainty in the  $C_{\ell}^{\text{GWGW}}(f)$  and  $C_{\ell}^{\text{gGW}}(f)$  is given by Eq. (12) and Eq. (15) respectively. The noise angular power spectrum,  $N_{\ell}$ , is derived in Appendix. A). In this analysis, we assume an isotropic distribution of pulsars with same noise characteristics for all pulsars. However, the formalism can be easily extended for any pulsar distribution. For this work, we set the noise parameters as  $A_{\text{rd}} = 10^{-14}$ ,  $\gamma = -2.5$ ,  $\sigma_w = 1 \times 10^{-7}$  sec, a pulse timing cadence of  $\Delta t = 30$  days, and a total observation duration of 20 years. These values are motivated by the noise characteristics observed in current PTA experiments (Agazie et al. 2023b). A realistic anisotropic distribution of pulsars will introduce additional complexities and decrease the sensitivity to the GW signal. In particular, anisotropy in the pulsar distribution affects the response function of the PTA, leading to

a directional dependence in the signal-to-noise ratio across the sky. This can impact the detectability of anisotropic features in the SGWB.

We perform a Fisher analysis for three distinct cases: (1) using  $\Omega_{\text{GW}}(f)$  alone, (2) combining  $\Omega_{\text{GW}}(f)$  and  $C_{\ell}^{\text{GWGW}}(f)$ , and (3) incorporating  $\Omega_{\text{GW}}(f)$ ,  $C_{\ell}^{\text{gGW}}(f)$ , and  $C_{\ell}^{\text{GWGW}}(f)$ . The analysis focuses on constraining the parameters,  $\eta$ ,  $\rho$ ,  $\nu$ ,  $\alpha$ , and  $\lambda$ . The parameters  $\mathcal{N}$  quantify the occupation fraction of the SMBHBs in galaxies. This parameter is completely degenerate with  $\eta$ ,  $\rho$ , and  $\nu$  as all of these control the overall magnitude of the  $\Omega_{\text{GW}}$ . We can fix the value to the  $\Omega_{\text{GW}}(f_{\text{ref}})$ , where  $f_{\text{ref}}$  can be the most sensitive frequency.

In Fig. 7, we present the results of the Fisher analysis for the three cases under consideration. We assume an array of 2000 isotropically distributed pulsars with identical noise properties. The injected parameter values are  $\eta = 8$ ,  $\nu = -0.3$ ,  $\alpha = -2.6$ , and  $\lambda = 0.3$ . The contour plots indicate that when only  $\Omega_{\text{GW}}(f)$  is used, no meaningful constraints can be placed on any parameters due to significant degeneracies, particularly between  $\eta$  and  $\rho$  with  $\nu$ . The  $M_* - M_{\text{BH}}$  relation cannot be directly measured with the SGWB, as it primarily probes the population properties of SMBH binaries rather than individual host galaxy correlations. The SGWB spectrum reflects the binary distribution over cosmic time, and additional constraints, such as the detection of individual GW sources and its host galaxy can help in breaking the degeneracies. The inclusion of the cross-correlation spectrum  $C_{\ell}^{\text{gGW}}(f)$  improves the constraints on the spectral parameters  $\alpha$ ,  $\lambda$ , and particularly on  $\nu$ . When the auto-correlation  $C_{\ell}^{\text{GWGW}}(f)$  is also incorporated into the analysis, we observe significantly tighter constraints on both  $\alpha$  and  $\lambda$ .

Despite the high signal-to-noise ratio (SNR) with which  $\Omega_{\text{gW}}$  can be measured, strong parameter degeneracies significantly limit its constraining power. While  $C_{\ell}^{\text{GWGW}}$  alone does not constrain any individual parameter due to its shot-noise-dominated nature, its combination with  $\Omega_{\text{gW}}$  helps break these degeneracies and yields valuable constraints. This improvement arises from the distinct parameter correlations inherent in  $\Omega_{\text{gW}}$ ,  $C_{\ell}^{\text{gGW}}$ , and  $C_{\ell}^{\text{GWGW}}$ . This highlights the crucial role of anisotropy signals in breaking degeneracies related to the redshift evolution of the SMBHB population.

It is worth noting that  $C_{\ell}^{\text{gGW}}$  is unaffected by changes in the overall magnitude of the signal. However, it is sensitive to the redshift evolution of the GW source, as it depends on the relative contributions of GWs from different redshifts. As we discussed in Sec. 4 with Fig. 6, the observables are differently affected by changes in the  $\eta$  and  $\nu$ . While  $\eta$  does not affect the features of the  $C_{\ell}^{\text{gGW}}$ , the observables are significantly affected by the change in  $\nu$ . This sensitivity helps to break the degeneracies that exist between the parameters. The  $\alpha$  governs the distribution of SMBHBs emitting at different frequencies, while  $\lambda$  controls its redshift evolution. Tight constraints on these parameters imply that PTAs can effectively probe the frequency distribution and its evolution with cosmic time.

In Fig. 8, we illustrate the evolution of the SMBHB mass as a function of redshift, along with the corresponding 68% credible interval on the measurement of the  $\text{Log}_{10}(M_{\text{BH}}(z)/M_{\odot})$ , for two different PTA noise configurations: (i)  $A_{\text{rd}} = 10^{-14}$ ,  $\gamma = -2.5$ ,  $\sigma_w = 10^{-7}$  sec and (ii)  $A_{\text{rd}} = 10^{-15}$ ,  $\gamma = -2.5$ ,  $\sigma_w = 10^{-7}$  sec. The

black dashed line represents the injected values of the  $\text{Log}_{10}(M_{\text{BH}}(z)/M_{\odot})$ . The analysis considers two pulsar configurations: 2000 and 5000 pulsars. The injected parameter values are  $\eta = 8$ ,  $\nu = -0.3$ ,  $\alpha = -2.6$ , and  $\lambda = 0.3$ . The quantity  $M_{\text{BH}}$  represents the mean primary mass of the SMBHB, given by Eq. (4), residing in a galaxy with a stellar mass of  $M_* = 10^{11} M_{\odot}$ . The  $M_* - M_{\text{BH}}$  relation is modeled based on insights from simulations and observational studies (Reines & Volonteri 2015; Habouzit et al. 2021; Kozhikkal et al. 2024), which examine this correlation for both isolated and binary BHs. The typical values of  $\eta$  and  $\rho$  are constrained by these studies, with variations estimated to be within  $\sim 10\%$ . We adopt this as a prior to quantify the uncertainty in the redshift evolution of  $M_{\text{BH}}$ , applying Gaussian priors on both  $\eta$  and  $\rho$  with standard deviations equal to 10% of their fiducial values<sup>1</sup>. The shaded region in the figure represents the 68% confidence interval.

The results are presented for three cases: (1) considering only  $\Omega_{\text{GW}}$ , (2) including both  $\Omega_{\text{GW}}$  and  $C_{\ell}^{\text{gGW}}$ , and (3) incorporating  $\Omega_{\text{GW}}$ ,  $C_{\ell}^{\text{gGW}}$ , and  $C_{\ell}^{\text{gGWGW}}$ . Consistent with the parameter constraints discussed earlier, we find that adding  $C_{\ell}^{\text{gGW}}$  significantly enhances the measurement of the redshift evolution of  $M_{\text{BH}}$ , while including  $C_{\ell}^{\text{gGWGW}}(f)$  further refines these constraints. Our results indicate that, with the noise configuration considered here, the mean SMBH mass,  $M_{\text{BH}}$ , for a given stellar mass of the host galaxy, can be measured with a signal-to-noise ratio ( $\text{SNR} = M_{\text{BH}}(z)/\sigma_{M_{\text{BH}}}(z)$ ) ranging from 1 to 4 for 2000 pulsars and 1.5 to 10 for 5000 pulsars.

Similarly, Fig. 9 and Fig. 10, we present the redshift evolution of the frequency distribution, quantified by normalized  $\frac{dN}{df} \times \Delta f$ , under similar conditions as Fig. 8, at  $f = 6 \times 10^{-9}$  Hz and  $f = 3 \times 10^{-8}$  Hz, respectively. Here,  $\Delta f$  represents the frequency resolution which in this case corresponds to the 20 years of observation. As expected, the constraints on  $\alpha$  and  $\lambda$  lead to an increasingly precise determination of the redshift dependence of the GW sources when anisotropy observables are included. In both cases, the improvement is more pronounced when increasing the number of pulsars from 2000 to 5000, further demonstrating the potential of PTAs to probe the SMBHB population with higher precision. The results show that, with the noise configuration considered here, the frequency distribution can be measured with a signal-to-noise ratio ( $\text{SNR} = \frac{dN}{df_r}/\sigma_{\frac{dN}{df_r}}$ ) ranging from 5 to 80 for 2000 pulsars and from 15 to 190 for 5000 pulsars at  $f = 6 \times 10^{-9}$  Hz. Similarly, at  $f = 3 \times 10^{-8}$  Hz, the SNR ranges from 1.5 to 22 for 2000 pulsars and 3 to 55 for 5000 pulsars.

In Table. 1, we show the ratio of the Figure of Merit (FoM) for two cases (i)  $\Omega_{\text{GW}}$  combined with  $C_{\ell}^{\text{gGW}}$  and (ii) the combination of  $\Omega_{\text{GW}}$ ,  $C_{\ell}^{\text{gGW}}$ , and  $C_{\ell}^{\text{gGWGW}}$ , relative to the case with only  $\Omega_{\text{GW}}$ . The FoM, defined as the square root of the determinant of the Fisher matrix, quantifies the information content and effectiveness of parameter estimation. The table compares the FoM ratio for different noise configurations and different numbers of isotropically distributed pulsars. From the table, we observe that adding the  $C_{\ell}^{\text{gGW}}$  to  $\Omega_{\text{GW}}$  enhances the FoM by a factor ranging from 1.8 to 2.5,

depending on the noise level and the number of pulsars. This indicates that including anisotropic features significantly improves the precision of parameter estimation. Furthermore, incorporating the SGWB auto-correlation term ( $C_{\ell}^{\text{gGWGW}}$ ) leads to a much more significant enhancement in FoM, with values increasing up to a factor of 17.8. This demonstrates the substantial gain in information when combining complementary information from  $\Omega_{\text{GW}}$ ,  $C_{\ell}^{\text{gGW}}$ , and  $C_{\ell}^{\text{gGWGW}}$ , as can be seen in Fig. 7. In the second and fourth columns of the table, the ratio of the FoM decreases because of the significant contribution from the cosmic variance term in  $C_{\ell}^{\text{gGW}}$  and  $C_{\ell}^{\text{gGWGW}}$ . With the decrease in the red noise or increase in the number of pulsars, the detection of all three quantities improves, but the dominance of the cosmic variance term in comparison to the noise term increases in the covariance matrix for  $C_{\ell}^{\text{gGW}}$  and  $C_{\ell}^{\text{gGWGW}}$ . As a result, the ratio of FoM with respect to the  $\Omega_{\text{GW}}$  at the same noise configurations decreases.

These results demonstrate that next-generation PTAs, such as SKA with its planned large number of pulsars, will be capable of providing meaningful constraints on the SMBHB population and its redshift evolution. Specifically, our Fisher analysis reveals that while the spectral energy density,  $\Omega_{\text{GW}}(f)$ , alone suffers from strong parameter degeneracies, the inclusion of anisotropic observables such as the angular power spectrum,  $C_{\ell}^{\text{gGWGW}}(f)$ , and the cross-angular power spectrum with galaxy surveys,  $C_{\ell}^{\text{gGW}}(f)$ , significantly improves parameter estimation.

These observables allow us to improve the measurement of key physical parameters, such as the redshift evolution of the SMBHB-Galaxy relation and the frequency distribution of the binaries, thereby refining our understanding of their cosmic history. Notably, our analysis indicates that constraints on the redshift evolution of SMBHBs are particularly sensitive to cross-correlation measurements, highlighting the crucial role of galaxy surveys in breaking degeneracies. By integrating future PTA datasets, such as those from SKA, with large-scale structure surveys, these constraints can be further refined, providing deeper insights into the formation and growth of SMBHBs across cosmic time.

While our analysis demonstrates the potential of PTAs in constraining the SMBHB population, several caveats must be considered. First, the sensitivity of PTAs is inherently limited by the number of pulsars, their spatial distribution, and the precision of timing residual measurements. Any unmodeled noise sources, such as intrinsic pulsar spin irregularities, could introduce biases in parameter estimation. Additionally, our approach assumes an idealized PTA with isotropically distributed pulsars with uniform noise properties, whereas real PTAs have anisotropically distributed pulsars with varying levels of timing precision. However, the anisotropic distribution of pulsars does not pose a fundamental issue for the analysis. While it introduces directionally dependent noise in the timing residual measurements, this primarily affects the angular resolution of the signal.

Future improvements will focus on incorporating realistic pulsar distributions and spatially varying noise models to refine our predictions. Additionally, deeper galaxy surveys with spectroscopic redshifts, such as Rubin LSST (Ivezić et al. 2019), DESI (Flaugher & Bebek 2014; Levi et al. 2013) and Euclid (Laureijs et al. 2010; Racca et al. 2016), will significantly enhance the cross-correlation analysis by pro-

<sup>1</sup> Results with 20% standard deviation on the priors of these parameters are presented in Appendix. B

SGWB signals used for the Analysis	Ratio of Figure of Merit (FoM) with respect to $\Omega_{\text{GW}}$			
	$A_{\text{rd}} = 10^{-14} N_p = 2000$	$A_{\text{rd}} = 10^{-15} N_p = 2000$	$A_{\text{rd}} = 10^{-14} N_p = 5000$	$A_{\text{rd}} = 10^{-15} N_p = 5000$
$\Omega_{\text{GW}} + C_{\ell}^{\text{gGW}}$	2.5	2.1	2.2	1.8
$\Omega_{\text{GW}} + C_{\ell}^{\text{gGW}} + C_{\ell}^{\text{gWGW}}$	12.7	14.5	16	17.8

**Table 1.** Table showing the ratios of Figure of Merit (FoM) for different cases with respect to the case with only  $\Omega_{\text{gW}}$  for different noise amplitudes and the number of isotopically distributed pulsars.

viding more precise three-dimensional maps of the galaxy distribution. This will allow for a more accurate determination of the redshift evolution of the SMBHB population. The combination of improved PTAs and more detailed galaxy surveys will ultimately enable a more robust understanding of the connection between SMBHBs and large-scale structures.

## 7 CONCLUSION

The nHz GW provides a unique probe for understanding the formation and evolution of SMBHBs. The detection of the SGWB by PTAs offers an opportunity to study the unresolved SMBHB population and its connection to galaxy evolution. In this work, we have demonstrated the feasibility of using the SGWB and its anisotropy to constrain the population and evolution of SMBHBs. By analyzing the spectral density of the SGWB,  $\Omega_{\text{GW}}(f)$ , its angular power spectrum,  $C_{\ell}^{\text{gGW}}(f)$ , and its cross-angular power spectrum with galaxy density fluctuations,  $C_{\ell}^{\text{gWGW}}(f)$ , we have explored the ability of PTAs to probe the SMBHB population properties and their redshift evolution. We show that anisotropic SGWB measurements significantly improve parameter estimation and break degeneracies in SMBHB population modeling.

Our Fisher analysis shows that  $\Omega_{\text{GW}}(f)$  alone offers limited constraining power due to parameter degeneracies, particularly between the SMBHB mass distribution parameters ( $\eta$  and  $\rho$ ) and its redshift evolution ( $\nu$ ). However, incorporating  $C_{\ell}^{\text{gWGW}}(f)$  and  $C_{\ell}^{\text{gGW}}(f)$  substantially improves these constraints, with  $C_{\ell}^{\text{gGW}}(f)$  being especially effective in breaking degeneracies linked to the redshift evolution of the SMBHB mass function. To further address the degeneracy between  $\eta$  and  $\rho$ , we impose 10% Gaussian priors on both, motivated by local observations of the  $M_* - M_{\text{BH}}$  relation. For a PTA with 5000 pulsars—achievable with the SKA—we find that the mean SMBHB mass corresponding to a given stellar mass can be measured with an SNR between 1.5 and 10, assuming the model holds across redshifts. Similarly, the frequency distribution can be constrained with an SNR ranging from approximately 5 to 190 over the same redshift interval. These findings underscore the promise of future PTAs in probing the cosmic evolution of the SMBHB population with exceptional precision.

Our results establish a benchmark for future studies of SMBHB populations using PTAs and galaxy surveys. Next-generation PTAs, such as SKA, with their increased number of pulsars and improved noise sensitivity, will provide better constraints on the SMBHB population. Additionally, future galaxy surveys like Rubin LSST, with improved redshift

accuracy, will refine the cross-correlation analysis. Incorporating multi-frequency GW observations from space-based detectors like LISA will further complement PTA measurements by probing SMBHBs across a broader mass and redshift range. These advancements will provide a more comprehensive picture of the formation and evolution of SMBHB.

## ACKNOWLEDGMENTS

This work is part of the `<data|theory>` Universe-Lab which is supported by the TIFR and the Department of Atomic Energy, Government of India. The authors would like to thank the `<data|theory>` Universe-Lab for providing computing resources. The author thanks Chiara Mingarelli and Federico Semenzato for their valuable feedback during NANOGrav paper circulation. The authors would also like to acknowledge the use of the following Python packages in this work: Numpy (Van Der Walt et al. 2011), Scipy (Jones et al. 01), Matplotlib (Hunter 2007), Astropy (Robitaille et al. 2013; Price-Whelan et al. 2018), Hasasia (Hazboun et al. 2019), Ray (Moritz et al. 2018), Pygic (Bocquet & Carter 2019), and PTArcade (Mitridate et al. 2023; Lamb et al. 2023).

## REFERENCES

- Agazie G., et al., 2023a, *The Astrophysical Journal Letters*, 952, L37
- Agazie G., et al., 2023b, *The Astrophysical Journal Letters*, 956, L3
- Anholm M., Ballmer S., Creighton J. D., Price L. R., Siemens X., 2009, *Physical Review D—Particles, Fields, Gravitation, and Cosmology*, 79, 084030
- Antoniadis J., et al., 2023, arXiv preprint arXiv:2306.16214
- Bocquet S., Carter F. W., 2019, *Astrophysics Source Code Library*, pp ascl-1907
- Burke-Spolaor S., et al., 2019, *The Astronomy and astrophysics review*, 27, 1
- Carretero J., et al., 2017, *PoS EPSHEP2017*, 488
- Chamberlin S. J., Creighton J. D., Siemens X., Demorest P., Ellis J., Price L. R., Romano J. D., 2015, *Physical Review D*, 91, 044048
- Chen S., Sesana A., Del Pozzo W., 2017, *Monthly Notices of the Royal Astronomical Society*, 470, 1738
- Christensen N., 2018, *Reports on Progress in Physics*, 82, 016903
- Cramér H., 1946, *Scandinavian Actuarial Journal*, 1946, 85
- Desvignes G., et al., 2016, *Monthly Notices of the Royal Astronomical Society*, 458, 3341
- Di Marco V., Zic A., Shannon R. M., Thrane E., 2024, *Monthly Notices of the Royal Astronomical Society*, 532, 4026
- Falxa M., et al., 2024, *Physical Review D*, 109, 123010

- Feng Y., Li D., Zheng Z., Tsai C.-W., 2020, *Physical Review D*, 102, 023014
- Fisher R. A., 1935, *Journal of the royal statistical society*, 98, 39
- Flaugher B., Bebek C., 2014, in *Ground-based and Airborne Instrumentation for Astronomy V*. pp 282–289
- Goncharov B., et al., 2021, *Monthly Notices of the Royal Astronomical Society*, 502, 478
- Habouzit M., et al., 2021, *Monthly Notices of the Royal Astronomical Society*, 503, 1940
- Hazboun J., Romano J., Smith T., 2019, *Journal of Open Source Software*, 4, 1775
- Hobbs G., Dai S., 2017, *National Science Review*, 4, 707
- Hunter J. D., 2007, *Computing in science & engineering*, 9, 90
- Ivezić Ž., et al., 2019, *The Astrophysical Journal*, 873, 111
- Izquierdo-Villalba D., Sesana A., Bonoli S., Colpi M., 2022, *Monthly Notices of the Royal Astronomical Society*, 509, 3488
- Jones E., Oliphant T., Peterson P., et al., 2001–, *SciPy: Open source scientific tools for Python*, <http://www.scipy.org/>
- Joshi B. C., et al., 2018, *Journal of Astrophysics and Astronomy*, 39, 51
- Kelley L. Z., Blecha L., Hernquist L., 2017, *Monthly Notices of the Royal Astronomical Society*, 464, 3131
- Kozhikkal M. M., Chen S., Theureau G., Habouzit M., Sesana A., 2024, *Monthly Notices of the Royal Astronomical Society*, 531, 1931
- Lamb W. G., Taylor S. R., van Haasteren R., 2023, *The Need For Speed: Rapid Refitting Techniques for Bayesian Spectral Characterization of the Gravitational Wave Background Using PTAs* (arXiv:2303.15442)
- Latif M. A., Ferrara A., 2016, *Publications of the Astronomical Society of Australia*, 33, e051
- Laureijs R. J., Duvel L., Sanz I. E., Gondoin P., Lumb D. H., Oosterbroek T., Criado G. S., 2010, in *Space Telescopes and Instrumentation 2010: Optical, Infrared, and Millimeter Wave*. pp 453–458
- Levi M., et al., 2013, arXiv preprint arXiv:1308.0847
- Lower M. E., et al., 2020, *Monthly Notices of the Royal Astronomical Society*, 494, 228
- Maiorano M., De Paolis F., Nucita A. A., 2021, *Symmetry*, 13, 2418
- Manchester R., et al., 2013, *Publications of the Astronomical Society of Australia*, 30, e017
- McLaughlin M. A., 2013, *Classical and Quantum Gravity*, 30, 224008
- Mingarelli C. M., Sidery T., Mandel I., Vecchio A., 2013, *Physical Review D—Particles, Fields, Gravitation, and Cosmology*, 88, 062005
- Mitra S., Dhurandhar S., Souradeep T., Lazzarini A., Mandic V., Bose . f. S., Ballmer S., 2008, *Physical Review D—Particles, Fields, Gravitation, and Cosmology*, 77, 042002
- Mitridate A., Wright D., von Eckardstein R., Schröder T., Nay J., Olum K., Schmitz K., Trickle T., 2023, arXiv preprint arXiv:2306.16377
- Moritz P., et al., 2018, in *13th USENIX symposium on operating systems design and implementation (OSDI 18)*. pp 561–577
- Padmanabhan H., Loeb A., 2023, *Astronomy & Astrophysics*, 676, A115
- Phinney E., 2001, arXiv preprint astro-ph/0108028
- Price-Whelan A. M., et al., 2018, *The Astronomical Journal*, 156, 123
- Racca G. D., et al., 2016, in *Space telescopes and instrumentation 2016: optical, infrared, and millimeter wave*. pp 235–257
- Raidal J., Urrutia J., Vaskonen V., Veermäe H., 2024, arXiv preprint arXiv:2411.19692
- Rao C. R., 1945, *Reson. J. Sci. Educ*, 20, 78
- Reardon D. J., et al., 2023, *The Astrophysical Journal Letters*, 951, L7
- Reines A. E., Volonteri M., 2015, *The Astrophysical Journal*, 813, 82
- Robitaille T. P., et al., 2013, *Astronomy & Astrophysics*, 558, A33
- Sah M. R., Mukherjee S., 2024, arXiv preprint arXiv:2407.11669
- Sah M. R., Mukherjee S., 2025, arXiv preprint arXiv:2501.01499
- Sah M. R., Mukherjee S., Saedzadeh V., Babul A., Tremmel M., Quinn T. R., 2024, arXiv preprint arXiv:2404.14508
- Sampson L., Cornish N. J., McWilliams S. T., 2015, *Physical Review D*, 91, 084055
- Sato-Polito G., Kamionkowski M., 2024, *Physical Review D*, 109, 123544
- Sato-Polito G., Zaldarriaga M., Quataert E., 2025, arXiv preprint arXiv:2501.09786
- Sesana A., Vecchio A., Colacino C. N., 2008, *Monthly Notices of the Royal Astronomical Society*, 390, 192
- Tallada P., et al., 2020, *Astronomy and Computing*, 32, 100391
- Tegmark M., Taylor A. N., Heavens A. F., 1997, *The Astrophysical Journal*, 480, 22
- Thrane E., Ballmer S., Romano J. D., Mitra S., Talukder D., Bose . f. S., Mandic V., 2009, *Physical Review D—Particles, Fields, Gravitation, and Cosmology*, 80, 122002
- Van Der Walt S., Colbert S. C., Varoquaux G., 2011, *Computing in science & engineering*, 13, 22
- Volonteri M., 2007, in *Relativistic Astrophysics Legacy and Cosmology—Einstein’s: Proceedings of the MPE/USM/MPA/ESO Joint Astronomy Conference Held in Munich, Germany, 7-11 November 2005*. pp 174–182
- Volonteri M., 2010, *The Astronomy and Astrophysics Review*, 18, 279
- Volonteri M., Habouzit M., Colpi M., 2021, *Nature Reviews Physics*, 3, 732
- Xu H., et al., 2023, arXiv preprint arXiv:2306.16216
- Zic A., et al., 2023, *Publications of the Astronomical Society of Australia*, pp 1–15

## APPENDIX A: DERIVATION OF THE NOISE ANGULAR POWER SPECTRUM

The cross-correlation of Fourier transform of the timing residuals from two pulsars I and J is given by:

$$\langle \tilde{r}_I(f) \tilde{r}_J^*(f) \rangle = B(f) \times \int d\hat{\Omega} \Omega_{\text{gw}}(f, \hat{\Omega}) \left( \mathcal{F}_I^+(\hat{\Omega}) \mathcal{F}_J^+(\hat{\Omega}) + \mathcal{F}_I^\times(\hat{\Omega}) \mathcal{F}_J^\times(\hat{\Omega}) \right), \quad (\text{A1})$$

where  $B(f) = 4\pi \frac{3H_0^2}{8\pi^4} \frac{f^{-5}}{\Delta f}$  and

$$\mathcal{F}_{i,k}^A = \frac{1}{2} \frac{\hat{p}_i^a \hat{p}_i^b}{1 + \hat{n}_k \cdot \hat{p}_i} e_{ab}^A. \quad (\text{A2})$$

The overlap reduction function between pulsars I and J,  $\Gamma_{IJ}$ , in an equal-pixel basis, called radiometer basis (Mitra et al. 2008; Thrane et al. 2009) is given by

$$\Gamma_{IJ} = \sum_k \Omega_{\text{gw},k} \left( \mathcal{F}_{I,k}^+(\hat{\Omega}) \mathcal{F}_{J,k}^+(\hat{\Omega}) + \mathcal{F}_{I,k}^\times(\hat{\Omega}) \mathcal{F}_{J,k}^\times(\hat{\Omega}) \right). \quad (\text{A3})$$

We can represent this in a matrix form as

$$\mathbf{\Gamma} = \mathbf{R} \mathbf{\Omega}, \quad (\text{A4})$$

where  $\mathbf{R}_k^{IJ} = \Omega_{\text{gw},k} \left[ \sum_A \mathcal{F}_{I,k}^A \mathcal{F}_{J,k}^A \right]$  and  $\mathbf{\Omega}_k = \Omega_{\text{gw},k}$

$$\mathcal{P}(\hat{\mathbf{X}}|\mathbf{\Omega}) \propto \exp\left[-\frac{1}{2} (\hat{\mathbf{X}}(f) - \mathbf{R}\mathbf{\Omega}(f))^T \Sigma^{-1} (f) (\hat{\mathbf{X}}(f) - \mathbf{R}\mathbf{\Omega}(f))\right], \quad (\text{A5})$$

where  $\hat{\mathbf{X}}_{IJ}(\mathbf{f}) = \tilde{r}_I(f)\tilde{r}_J^*(f)/B(f)$ ,  $\Sigma(f)$  is the cross-correlation covariance matrix.

The uncertainty in the measurement of  $\Omega_{\text{gw},k}$  denoted by  $\Sigma_{\text{pix}}$  is given by the square root of the diagonal terms in the inverse of Fisher matrix  $\mathbf{R}^T \Sigma^{-1} \mathbf{R}$  as

$$\Sigma_{\text{pix}}(f) = (\mathbf{R}^T \Sigma(\mathbf{f})^{-1} \mathbf{R})^{-1}. \quad (\text{A6})$$

For an isotropic distribution of pulsars with the same pulsar timing residual noise for every pulsar, the pixel noise covariance matrix,  $\Sigma_{\text{pix}}$  becomes diagonal and the noise angular power spectrum in this case can be written as

$$N_\ell = \frac{4\pi}{N_{\text{pix}}} \sigma_{\text{pix}}^2, \quad (\text{A7})$$

where,  $\sigma_{\text{pix}}$  is standard deviation of pixel noise.

## APPENDIX B: CONSTRAINT ON THE EVOLUTION OF THE SMBHB POPULATION

We demonstrate the results obtained in Sec. 6 for the redshift evolution of the SMBHB population with broader prior on  $\eta$  and  $\rho$ . We assume a Gaussian prior with a standard deviation equal to the 20% of the fiducial values of the  $\eta$  and  $\rho$ . Fig. B1 depicts the evolution of the SMBHB mass as a function of redshift, along with the associated uncertainty, for two different PTA noise configurations: (i)  $A_{\text{rd}} = 10^{-14}$ ,  $\gamma = -2.5$ ,  $\sigma_w = 10^{-7}$  sec and (ii)  $A_{\text{rd}} = 10^{-15}$ ,  $\gamma = -2.5$ ,  $\sigma_w = 10^{-7}$  sec. The analysis is conducted for two pulsar populations: 2000 and 5000 pulsars. With the noise configuration assumed here, our analysis shows that the mean SMBH mass ( $M_{\text{BH}}$ ) residing in the galaxy with a given stellar mass can be detected with an SNR ranging from 1 to 3 for 2000 pulsars and 1.5 to 5 for 5000 pulsars.

Similarly, Figs. 9 and 10 show the redshift evolution of the frequency distribution, represented by the normalized  $\frac{dN}{df} \times \Delta f$ , under same conditions. We find that frequency distribution can be measured with an SNR ranging from 5 to 80 for 2000 pulsars and from 12 to 190 for 5000 pulsars at  $f = 6 \times 10^{-9}$  Hz. Similarly, at  $f = 3 \times 10^{-8}$  Hz, the SNR ranges from 1.5 to 20 for 2000 pulsars and 3 to 55 for 5000 pulsars.



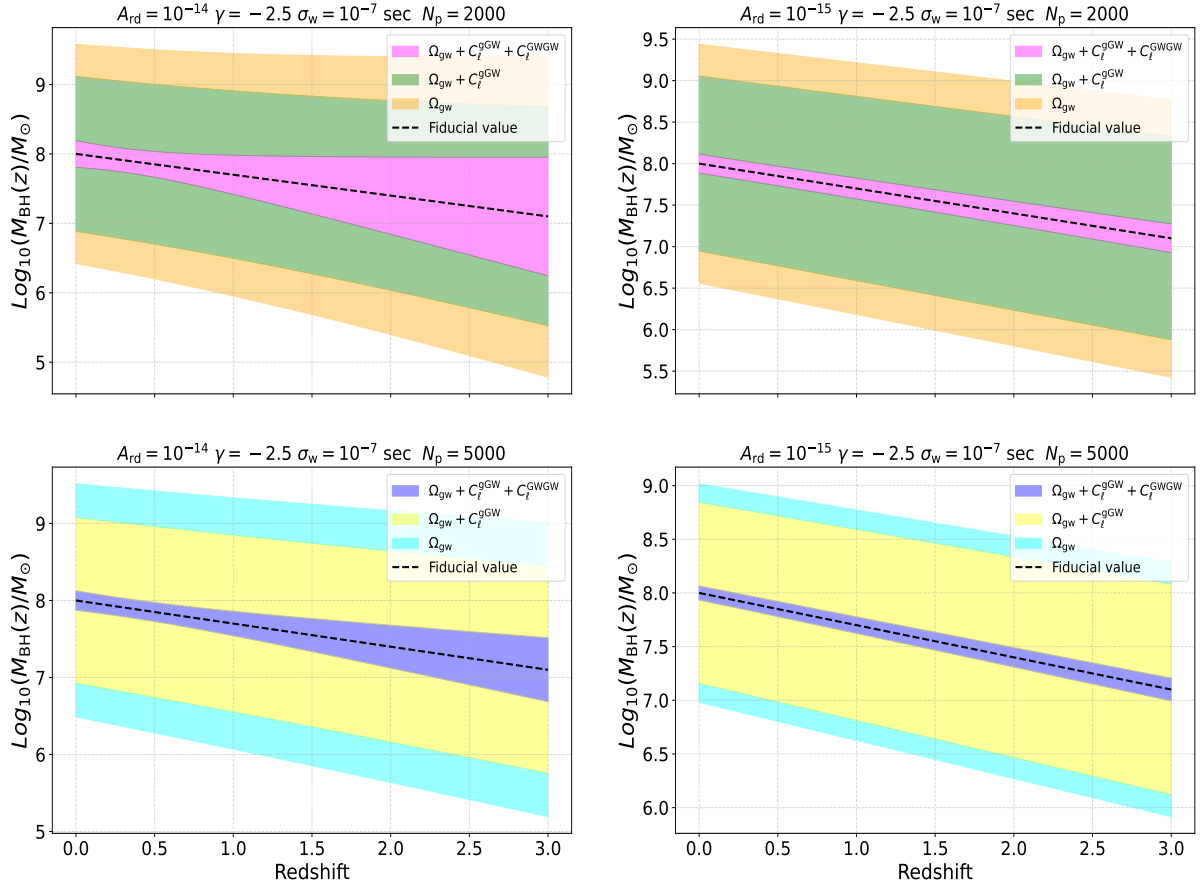


**Figure B1.** Evolution of the mean mass of the SMBHB ( $M_{\text{BH}}(z)$ ), given by Eq. (4), for a stellar mass of  $M_* = 10^{11} M_\odot$  as a function of redshift. The shaded regions represent the 68% credible interval on  $M_{\text{BH}}$ . The results are shown for two different PTA noise configurations: (i)  $A_{\text{rd}} = 10^{-14}$ ,  $\gamma = -2.5$ ,  $\sigma_w = 10^{-7}$  sec (left panel) and (ii)  $A_{\text{rd}} = 10^{-15}$ ,  $\gamma = -2.5$ ,  $\sigma_w = 10^{-7}$  sec (right panel). Each configuration is analyzed for  $N_p = 2000$  (upper panel) and  $N_p = 5000$  (lower panel) pulsars. The injected parameter values are  $\eta = 8$ ,  $\nu = -0.3$ ,  $\alpha = -2.6$ , and  $\lambda = 0.3$ . A Gaussian prior is applied to  $\eta$  and  $\rho$ , with a standard deviation of 20% of their injected values. The results are presented for three cases: (1) considering only  $\Omega_{\text{GW}}$ , (2) including both  $\Omega_{\text{GW}}$  and  $C_\ell^{\text{gGW}}$ , and (3) incorporating  $\Omega_{\text{GW}}$ ,  $C_\ell^{\text{gGW}}$ , and  $C_\ell^{\text{gGWG}}$ .

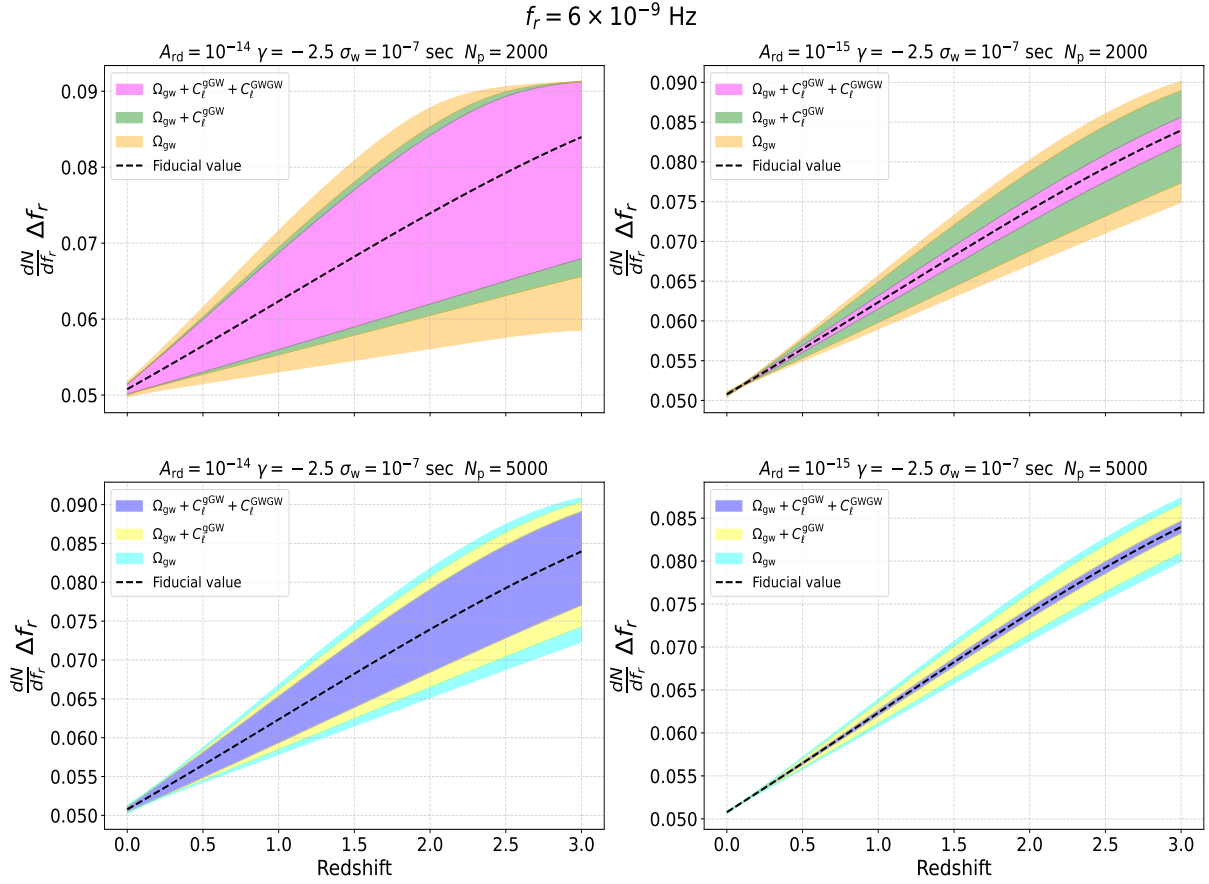


**Figure B2.** Redshift evolution of the frequency distribution, normalized  $\frac{dN}{df_r} \times \Delta f_r$  at  $f_r = 6 \times 10^{-9}$  Hz, of SMBHBs as a function of redshift. The shaded regions represent the 68% credible interval. Results are shown for two different PTA noise configurations: (i)  $A_{\text{rd}} = 10^{-14}$ ,  $\gamma = -2.5$ ,  $\sigma_w = 10^{-7}$  sec (left panel) and (ii)  $A_{\text{rd}} = 10^{-15}$ ,  $\gamma = -2.5$ ,  $\sigma_w = 10^{-7}$  sec (right panel). Each configuration is analyzed for  $N_p = 2000$  (upper panel) and  $N_p = 5000$  (lower panel) pulsars. The injected parameter values are  $\eta = 8$ ,  $\nu = -0.3$ ,  $\alpha = -2.6$ , and  $\lambda = 0.3$ . A Gaussian prior is applied to  $\eta$  and  $\rho$ , with a standard deviation of 20% of their injected values. The results are presented for three cases: (1) considering only  $\Omega_{\text{GW}}$ , (2) including both  $\Omega_{\text{GW}}$  and  $C_\ell^{\text{gGW}}$ , and (3) incorporating  $\Omega_{\text{GW}}$ ,  $C_\ell^{\text{gGW}}$ , and  $C_\ell^{\text{GWWG}}$ .

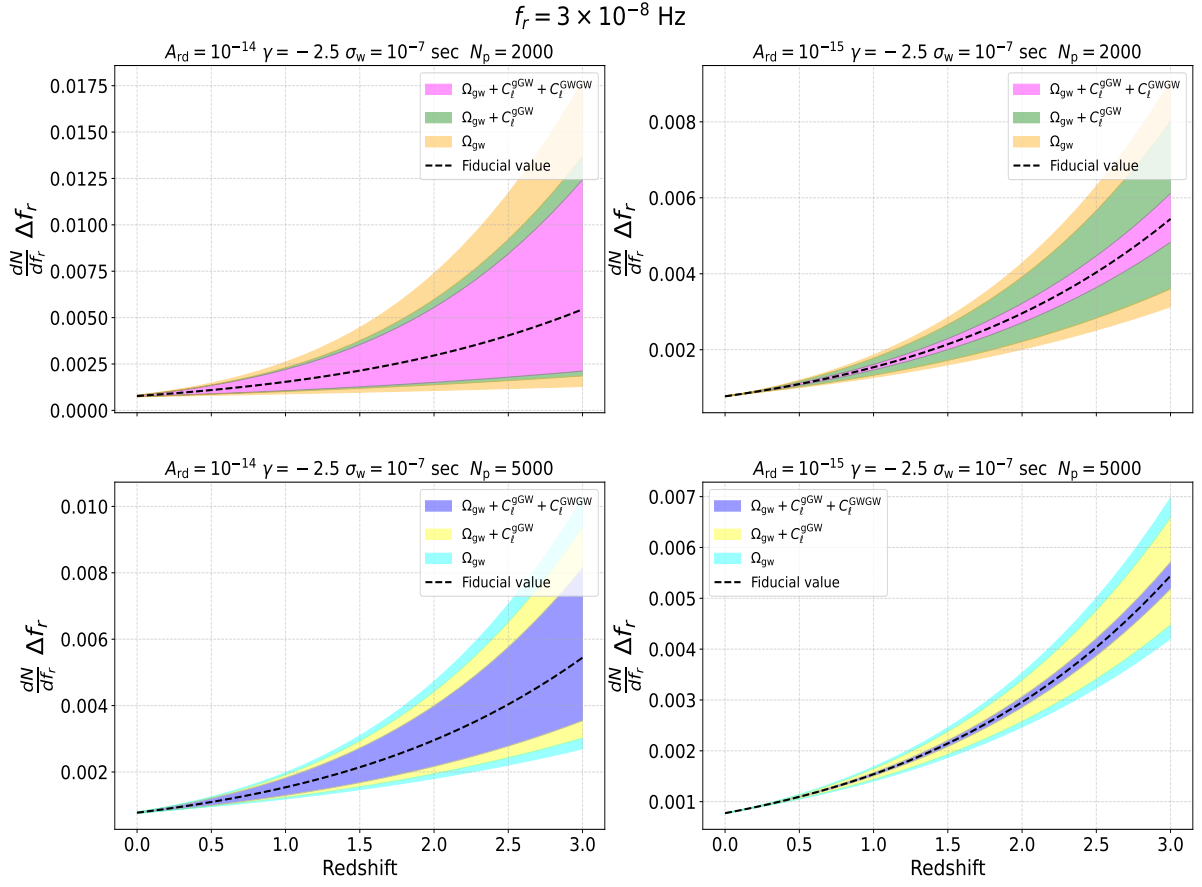


**Figure B3.** Redshift evolution of the frequency distribution, normalized  $\frac{dN}{df_r} \times \Delta f_r$  at  $f_r = 3 \times 10^{-8}$  Hz, of SMBHBs as a function of redshift. The shaded regions represent the 68% credible interval. Results are shown for two different PTA noise configurations: (i)  $A_{\text{rd}} = 10^{-14}$ ,  $\gamma = -2.5$ ,  $\sigma_w = 10^{-7}$  sec (left panel) and (ii)  $A_{\text{rd}} = 10^{-15}$ ,  $\gamma = -2.5$ ,  $\sigma_w = 10^{-7}$  sec (right panel). Each configuration is analyzed for  $N_p = 2000$  (upper panel) and  $N_p = 5000$  (lower panel) pulsars. The injected parameter values are  $\eta = 8$ ,  $\nu = -0.3$ ,  $\alpha = -2.6$ , and  $\lambda = 0.3$ . A Gaussian prior is applied to  $\eta$  and  $\rho$ , with a standard deviation of 20% of their injected values. The results are presented for three cases: (1) considering only  $\Omega_{\text{GW}}$ , (2) including both  $\Omega_{\text{GW}}$  and  $C_\ell^{\text{gGW}}$ , and (3) incorporating  $\Omega_{\text{GW}}$ ,  $C_\ell^{\text{gGW}}$ , and  $C_\ell^{\text{gGWG}}$ .